Chemical Geology 584 (2021) 120535

Contents lists available at ScienceDirect

Chemical Geology

journal homepage: www.elsevier.com/locate/chemgeo

Helium-carbon systematics of groundwaters in the Lassen Peak Region

Peter H. Barry [a,*], David V. Bekaert [a], John A. Krantz [a], Sæmundur A. Halldórsson [b], J. M. de Moor [c], Tobias P. Fischer [d], Cynthia Werner [e], Peter J. Kelly [f], Alan M. Seltzer [a], Brian P. Franz [g], Justin T. Kulongoski [g,h]

[a] Marine Chemistry and Geochemistry Department, Woods Hole Oceanographic Institution, Woods Hole, MA, USA
[b] Nordic Volcanological Center, Institute of Earth Sciences, University of Iceland, Sturlugata 7, 102 Reykjavík, Iceland
[c] Observatorio Volcanológico y Sismológico de Costa Rica (OVSICORI), Universidad Nacional, Costa Rica
[d] Department of Earth and Planetary Sciences, University of New Mexico, Albuquerque, NM, USA
[e] U.S. Geological Survey Contractor, 392 Tukapa St., RD1, New Plymouth 4371, NZ, USA
[f] U.S. Geological Survey, Cascades Volcano Observatory, 1300 SE Cardinal Ct., Suite 100, Vancouver, WA 98683-9589, USA
[g] Scripps Institution of Oceanography, Geosciences Research Division, La Jolla, CA 92094, USA
[h] U.S. Geological Survey, California Water Science Center, San Diego, CA 92101, USA

ARTICLE INFO

Editor: Don Porcelli

Keywords:
Helium
Carbon
Lassen
Groundwater
Volcano
Isotopes

ABSTRACT

Carbon dioxide emissions from active subaerial volcanoes represent 20–50% of the annual global volcanic CO_2 flux (Barry et al., 2014). Passive degassing of carbon from the flanks of volcanoes, and the associated accumulation of dissolved inorganic carbon (DIC) within nearby groundwater, also represents a potentially important, yet poorly constrained flux of carbon to the surface (Werner et al., 2019). Here we investigate sources and sinks of DIC in groundwaters in the Lassen Peak region of California. Specifically, we report and interpret the relative abundance and isotopic composition of helium (^{3}He, ^{4}He) and carbon (^{12}C, ^{13}C, ^{14}C) in 37 groundwater samples, from 24 distinct wells, collected between 20 and 60 km from Lassen Peak. Measured groundwater samples have air-corrected ^{3}He/^{4}He values between 0.19 and 7.44 R_A (where R_A = air ^{3}He/^{4}He = 1.39×10^{-6}), all in excess of the radiogenic production value (~0.05 R_A), indicating pervasive mantle-derived helium additions to the groundwater system in the Lassen Peak region. Stable carbon isotope ratios of DIC (δ^{13}C) vary between −12.6 and − 27.7‰ (vs. VPDB). Measured groundwater DIC/^{3}He values fall in the range of 2.2×10^{10} to 1.1×10^{12}. Using helium and carbon isotope data, we explore several conceptual models to estimate surface carbon contributions and to differentiate between DIC derived from soil CO_2 versus DIC derived from external (slab and mantle) carbon sources. Specifically, if we use ^{14}C to identify soil-derived DIC (assuming decadal-to-centennial groundwater ages and a soil CO_2 ^{14}C activity equal to that of the atmosphere), we calculate that a hypothetical external carbon source would have an apparent δ^{13}C signature between −10.3 and − 59.3‰ (vs. Vienna Pee Dee Belemnite (VPDB)) and an apparent C/^{3}He between 7.0×10^9 and 1.0×10^{12}. These apparent δ^{13}C and C/^{3}He values are substantially isotopically lighter than and greater than canonical MORB values, respectively. We suggest that >95% of any external (non-soil-derived) DIC in groundwater must thus be non-mantle in origin (i.e., slab derived or assimilated organic carbon). We further investigate possible sources of external DIC to groundwater using two idealized conceptual approaches: a pure (unfractionated) source mixing model (after Sano and Marty, 1995) and a scenario that invokes fractionation due to calcite precipitation. Because the former model requires carbon contributions from an organic source component with unrealistically low δ^{13}C (~ − 60‰), we suggest that the second scenario is more plausible. Importantly, however, we caution that all conceptual models are dependent on assumptions about initial ^{14}C activity. Thus, we cannot rule out the possibility that the true fraction of non-surface-derived DIC in these samples is lower or negligible, despite the pervasive mantle-derived He isotope signatures throughout the region. Following the ^{14}C approach to deconvolving sources of DIC, we determine that the maximum passive carbon flux could be up to ~2.2×10^6 kg/yr, which is lower than previous magmatic carbon flux estimates from the Lassen region (Rose and Davisson, 1996). We find that the passive dissolved carbon flux could represent a maximum of ~4–18% of the total Lassen geothermal CO_2 degassing flux (estimated to be ~3.5×10^7 kg/yr Rose and Davisson, 1996; Gerlach et al.,

* Corresponding author.
E-mail address: pbarry@whoi.edu (P.H. Barry).

https://doi.org/10.1016/j.chemgeo.2021.120535
Received 5 April 2021; Received in revised form 1 September 2021; Accepted 19 September 2021
Available online 23 September 2021

2008), which is still more than an order of magnitude smaller than soil gas CO_2 flux estimates (7.3–11 × 10^7 kg/yr) for nearby volcanoes (Sorey et al., 1998; Gerlach et al., 1999; Evans et al., 2002; Werner et al., 2014). We conclude that passive dissolved carbon fluxes should be combined with geothermal fluxes and soil gas fluxes to obtain a complete picture of volcanic carbon emissions globally. Our approach highlights the utility of measuring helium isotopes in concert with the full suite of noble gas abundances, tritium, $\delta^{13}C$ and ^{14}C, which when interpreted together can be used to better elucidate the various sources of DIC in groundwater.

1. Introduction

Noble gases and stable isotopes have long been used to characterize sources, fluxes and pathways of carbon through volcanic groundwater systems (Rose et al., 1996; Rose and Davisson, 1996; Allard et al., 1997; Davisson and Rose, 1997; James et al., 1999; Chiodini et al., 1999; Chiodini et al., 2000; James et al., 2000; Evans et al., 2002; Saar et al., 2005; Barry et al., 2013; Werner et al., 2013; Bergfeld et al., 2017; Barry et al., 2019a; Barry et al., 2019b), and many previous studies have documented summit degassing, referred to as active degassing (Marty et al., 1989; Gerlach, 1991; Marty and Le Cloarec, 1992; Williams et al., 1992; Sano and Williams, 1996; Gerlach et al., 2008). However, diffuse soil degassing and dissolved carbon emissions from the flanks and areas surrounding volcanoes, referred to as passive degassing, have historically been less studied (e.g., Rose and Davisson, 1996; Chiodini et al., 2000, 2004; Crossey et al., 2009; Fischer et al., 2019; Aiuppa et al., 2019; Werner et al., 2019). The most well studied mechanisms for deep (i.e., mantle- and subduction-derived) volatile transport to shallow groundwater is tectonic activity and transport along active faults (e.g., Lupton, 1983; Oxburgh et al., 1986; Oxburgh and O'Nions, 1987; Kennedy et al., 1997; Kulongoski et al., 2005, 2013; Crossey et al., 2016), but the processes associated with diffusive transport of volatiles remain poorly constrained (Lee et al., 2016; Werner et al., 2019). Comprehensive studies of passive magmatic degassing through groundwater on volcanic flanks have the potential to significantly improve our understanding of carbon fluxes in volcanic domains worldwide (Werner et al., 2019).

Lassen Peak reaches an elevation of 3187 m and is the southernmost active volcano in the Cascade Range of the western United States (Fig. 1). It is located in northern California and is part of the Cascade Volcanic Arc, which stretches from southwestern British Columbia to northern California. The Hat Creek basin to the north of Lassen Peak (Fig. 1) has been extensively studied; notably, Rose et al. (1996) used stable isotopes ($\delta^{18}O$, δD, $\delta^{13}C$) and ^{14}C in the Hat Creek basin to identify areas of recharge, aquifer residence times, and flow paths. Their findings indicated a high level of aquifer interconnectivity between the recharge and discharge locations (Rose et al., 1996). The Hat Creek Basin aquifers, which are thought to interact with volcanic gases, have been estimated to transport approximately 10% to 20% of the total volcanic carbon flux from the Lassen Peak area as total dissolved inorganic carbon (DIC) (Rose et al., 1996). Davisson and Rose (1997) measured stable isotope and radiocarbon values for thermal springs and surface water samples throughout the Hat Creek region. They compared the Hat Creek area, the Medicine Lake volcano area to the north, and the Mt. Shasta area to the northwest, and concluded that laterally extensive Quaternary basalt flows of high permeability extending from the bases of the volcanoes provide conduits for groundwater and magmatic carbon to be transported away from high precipitation areas near the volcano summits (Davisson and Rose, 1997). Other previous studies have used helium and carbon isotopes as a means to understand groundwater flow in the southern Cascades of Oregon (James et al., 2000; Saar et al., 2005), as well as to characterize and quantify magmatic carbon emissions from cold springs (Evans et al., 2002) and geothermal systems (Hilton, 1996) in the Mammoth Mountain and Long Valley caldera regions (Bergfeld et al., 2006; Werner et al., 2014).

Here, we use dissolved helium isotope ratios ($^3He/^4He$), and carbon isotopes of DIC ($\delta^{13}C$ and ^{14}C) in groundwater, along with noble gas abundances (He, Ne, Ar, Kr, and Xe), and DIC speciation, to explore the provenance of carbon in the groundwater system of the Lassen Peak region (Kulongoski and Hilton, 2012). We adopt methods from the aforementioned studies and introduce a new idealized conceptual model to investigate carbon isotope variability as a function of calcite precipitation. Volatile geochemistry can be used to elucidate the extent of external (slab and mantle) gas interaction with groundwater, the role of groundwater systems in the dispersal of volcanically derived volatiles, and the role of volcanic regions in the deep carbon cycle.

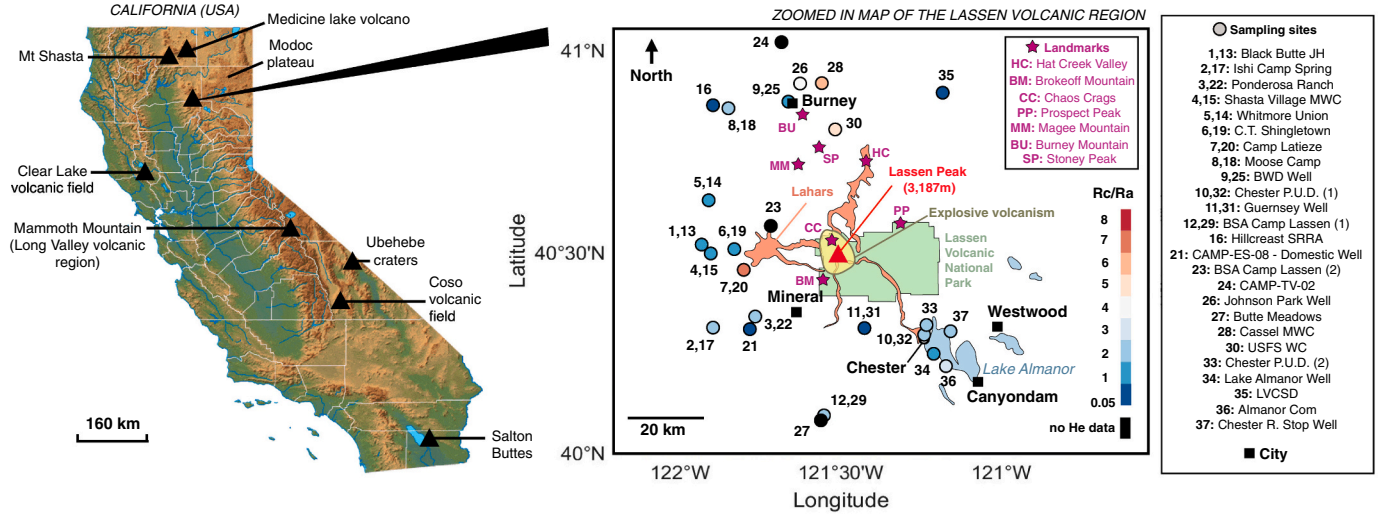

Fig. 1. Maps showing the Lassen Peak region, California, USA. The left panel shows the location of Lassen Peak relative to the entire state of California. The right panel shows a zoomed-in view of the Lassen region, including place names and locations. In total, 37 water samples were collected from 24 distinct wells, shown as colored dots on the figure. The color coding shows helium isotope (R_C/R_A) variations. The location of lahars and geological landmarks are also shown for reference.

2. Geologic background

Stretching from British Columbia to northern California, the Cascade Range marks the northeastern extent of the Pacific Rim of Fire. The Cascade Range formed in response to the subduction of the Juan de Fuca Plate beneath the North American Plate (Guffanti and Weaver, 1988). The Gorda micro plate forms a ~ 250 km long segment of the larger Juan de Fuca Plate (Walter, 1986; Cockerham, 1984) subducts beneath northern California. As a result, voluminous, intermediate to silicic volcanism of late Pliocene to Quaternary ages erupted at hundreds of volcanic vents that surround five longer-lived volcanic centers in the Lassen volcanic field (Guffanti and Weaver, 1988; Clynne, 1990).

Lassen Peak is located in northeastern California (Fig. 1), west of the Basin and Range province, and is the southernmost historically active volcano of the Cascade Range. It last erupted between 1914 and 1917, with the most notable (steam explosion) eruption on May 22, 1915. The 1915 event heavily impacted a 7.8 square-kilometer area to the northeast of the peak which is colloquially known as the Devastated Area. Today, the Lassen Peak volcanic system is still considered active, with a magma chamber capable of eruptions, hence representing a potential threat through lava/pyroclastic flows and lahars (volcanically induced mudslides, landslides, and debris flows; Fig. 1). Each year, large winter storms provide a voluminous snowpack that feeds into regional groundwater and hydrothermal systems (Ingebritsen et al., 2015, 2016; Ingebritsen and Evans, 2019). Cold springs located several kilometers from Lassen Peak are supplied by groundwater recharge from snowmelt near the summit (Muffler et al., 1982; Sorey and Ingebritsen, 1983), contributing a large portion of the annual storage in the Shasta Reservoir (Rose et al., 1996; Davisson and Rose, 1997). There are two separate hydrothermal cells driven by heat from the Lassen volcanic system (Janik and McLaren, 2010). Magmatic volatiles are released and dissolved into fluids within these hydrothermal cells, which represents the largest active hydrothermal system in the Cascades.

The region to the north of Lassen Peak is characterized by active *en echelon* normal faulting through volcanic bedrock of late Tertiary and Quaternary age (Wills, 1991). To the west, three prominent cinder cones (Magee Mountain, Stoney Peak, and Burney Mountain) form a chain of cones that terminates at Lassen Peak (Anderson, 1940). The clustering of volcanic vents in the region suggests that crustal extension prompted volcanism along north-northwest trending fault zones (Guffanti and Weaver, 1988). The Pit River marks the northernmost extent of surface and groundwater flow from Lassen Peak and eventually supplies water for the Shasta Reservoir. In this study, 24 wells were sampled at distances between 20 and 60 km from Lassen Peak (Fig. 1). The distribution of the wells allows for a general exploration of the distribution, character, and quantity of volcanically derived carbon to the regional groundwater systems around Lassen Peak.

3. Methods

3.1. Sampling methods

In total, 24 wells were sampled (13 in duplicate) to the north, west and south of Lassen Peak (Fig. 1) as part of a joint regional groundwater study between Scripps Institution of Oceanography (SIO) and the U.S. Geological Survey (USGS) in August through October 2010 (Tables 1-4). All wells were pumped prior to sampling until three casing volumes had been removed. Samples were not collected until temperature and pH stabilized. Water from the pump was then extracted through air tight Tygon® tubing into 3/8″ copper tubing and clamped at a fixed length of approximately 25 cm. The Tygon® tubing allows for identification and removal of unwanted bubbles prior to crimping the copper tubes. Copper tubes retain the integrity of water samples (even after extended storage) due to the extremely low permeability of helium through copper (Weiss, 1968).

To obtain field parameters, groundwater samples were pumped through a flow-through chamber fitted with a multi-probe meter that simultaneously measures dissolved oxygen, temperature, pH, and specific conductance (e.g., Wilde and Radtke, 1998). All sensors on the multi-probe meter were calibrated daily. Measured temperature, dissolved oxygen, pH, and specific conductance values were recorded at 5-min intervals for approximately 30 min, and when these values remained stable for 20 min, samples for laboratory analyses then were collected.

Groundwater samples collected for trace elements, major and minor ions, silica, and TDS analyses required filling one 250 mL polyethylene bottle with unfiltered groundwater, and one 500-mL and one 250-mL polyethylene bottle with filtered groundwater (Wilde and Radtke, 1998). Filtration was done using a 0.45-μm pore-size filter that was pre-rinsed with 2 L of deionized water, then rinsed with at least 1 L of groundwater prior to sampling. The 250 mL filtered sample then was preserved with 7.5-normal (7.5-N) nitric acid. Nutrient samples were collected by filtering groundwater into a 125 mL brown polyethylene bottle. Samples to be analyzed for stable isotopes of carbon in DIC and ^{14}C activity were filtered and bottom filled into 500 mL glass bottles that first were overfilled with three bottle volumes of groundwater. These samples had no headspace and were sealed with conical caps to avoid atmospheric contamination. Samples for laboratory or field alkalinity titrations were collected by filtering groundwater into a 500 mL polyethylene bottle.

Field alkalinity was measured at the well site on filtered samples by Gran's titration method (Gran, 1952). Titration data were used to calculate the concentrations of bicarbonate (HCO_3^-) and carbonate (CO_3^{2-}) using the advanced speciation method, with pK1 = 6.35, pK2 = 10.33, and pKW = 14. Concentrations of CO_2, HCO_3^- and CO_3^{2-} also were calculated (Dickson et al., 2003) from the laboratory alkalinity and laboratory pH measurements using CO2SYS software (Lewis and Wallace, 1998).

3.2. Analytical methods

The temperature, pH, and total dissolved solids of each sample were obtained using a YSI multimeter in the field. The concentrations of major cations (Ca^{+2}, Mg^{+2}, Na^+, and K^+) were measured using a Metrohm 850 Professional Ion Chromatograph (Table 4; EPA, 1993; Garbarino and Struzeski, 1998, Halldórsson et al., 2021). Major and minor ions, trace elements were measured using atomic absorption spectrometry, colorimetry, ion-exchange chromatography, inductively-coupled plasma atomic emission spectrometry and mass spectrometry (e.g., Fishman and Friedman, 1989; Garbarino et al., 2006).

A subset of water samples ($n = 12$) were processed for He, Ne and C isotopes at Scripps Institution of Oceanographic (SIO) using the Fluid Extraction, Noble Gas Separation, Quadrupole Mass-Spectrometer System (FENGS-QMS) (Kulongoski and Hilton, 2002). The remaining samples, including duplicate samples of those that were analyzed at SIO, were measured for the full suite of gases and tritium at Lawrence Livermore National Laboratory (LLNL) and for C isotopes at Woods Hole Oceanographic Institution (WHOI), National Ocean Sciences Accelerator Mass Spectrometry (NOSAMS) Facility.

At SIO the copper tube sample was connected to the sample release section of the line and pumped to high vacuum, at which point the clamp was opened and water was released into a degassing bulb that contained a small amount of phosphorus pentoxide to acidify the water, thus assisting gas extraction. The released gas was then expanded into a vacuum line where the water vapor was trapped at −78 °C. CO_2 was then captured on a U-tube by immersion in liquid nitrogen, while all remaining gases were transferred into the gas preparation section. In this section of the line, He and Ne were isolated by removing all active gases with a titanium sponge heated to ~700 °C, followed by trapping heavy noble gases on activated charcoal at a temperature of −196 °C (Kulongoski and Hilton, 2002). Once He and Ne were isolated, they were transferred to a Quadrupole Mass Spectrometer (QMS) where relative

Table 1
Helium and carbon characteristics.

Sample	Sample #	Lat	Long	pH	Temp (C)	R/R_A	Error	$^4He/^{20}Ne$	X-value[1]	Error	R_C/R_A (Eq. 2)[2]	Error	DIC (mol/L)[3]	$\delta^{13}C$ meas (permil vs VPDB)	$\delta^{13}C$ meas (Error)	$C/^3He$[4]
Black Butte JH	1	40.5179	−121.93336	6.3	12	1.19	0.03	0.32	1.27	0.005	1.92	0.06	2.25E-03	−21.9	0.6	2.52E+11
Ishi Camp Spring	2	40.3116	−121.8964	7.2	19	0.98	0.05	0.38	1.51	0.009	0.93	0.05	1.41E-03	−22.9	0.6	4.54E+11
Ponderosa Ranch	3	40.339	−121.76488	6.6	12.5	1.04	0.05	0.35	1.38	0.010	1.13	0.05	1.87E-03	−27.7	0.6	2.93E+11
Shasta Village MWC	4	40.49733	−121.9044	6.4	10.5	1.09	0.05	0.33	1.31	0.006	1.36	0.07	2.28E-03	−21.6	0.6	3.90E+11
Whitmore Union	5	40.62858	−121.91125	6.8	14	1.05	0.05	0.38	1.52	0.016	1.15	0.06	1.99E-03	−19.7	0.6	3.37E+11
C.T. Shingletown 1	6	40.50608	−121.83219	6.5	9	1.22	0.05	0.35	1.38	0.006	1.79	0.07	1.50E-03	−18.6	0.6	2.28E+11
Camp Latieze	7	40.456166	−121.80241	6.7	12	2.26	0.06	0.45	1.78	0.006	3.88	0.11	1.60E-03	−17.5	0.6	9.36E+10
Moose Camp	8	40.8562	−121.84833	7	8	1.36	0.04	0.33	1.31	0.011	2.52	0.08	8.09E-04	−20.4	0.6	1.16E+11
BWD Well #7	9	40.8713	−121.66036	7.6	8	1.00	0.04	0.34	1.36	0.005	1.00	0.04	6.00E-04	−20.6	0.6	1.02E+11
Chester P.U.D. #3	10	40.2939	−121.23913	7.3	8.5	1.28	0.04	0.35	1.37	0.005	2.04	0.06	9.16E-04	−23.6	0.6	1.17E+11
Guernsey Well	11	40.3094	−121.426333	8.5	14.5	0.74	0.06	0.46	1.81	0.006	0.42	0.03	4.49E-04	−27.4	0.6	4.98E+10
BSA Camp Lassen	12	40.09422	−121.55238	6.6	8.5	1.16	0.04	0.36	1.40	0.005	1.56	0.05	1.23E-03	−21.5	0.6	1.30E+11
Black Butte JH	13	40.51791667	−121.9333611	6.32	12	1.26	0.02	0.26	1.02	0.005			2.25E-03	−18.7	0.6	4.05E+11
Whitmore Union	14	40.62858333	−121.91125	6.79	14	1.04	0.02	0.29	1.15	0.006	1.33	0.04	1.99E-03	−19.9	0.6	5.50E+11
Shasta Village MWC	15	40.49733333	−121.9044167	6.44	10.5	1.07	0.01	0.24	0.97	0.005			2.28E-03	−20.7	0.6	6.38E+11
Hillcreast SRRA 1	16	40.86280556	−121.8965278	5.84	10	1.00	0.01	0.26	1.03	0.005	0.91	0.03	1.62E-03	−20.6	0.6	3.26E+11
Ishi Camp Spring	17	40.31163889	−121.8964722	7.23	19	0.93	0.03	0.24	0.95	0.005	2.33	0.07	1.41E-03	−18.5	0.6	1.11E+12
Moose Camp	18	40.85625	−121.8483333	7.01	8	0.97	0.01	0.35	1.39	0.007	0.89	0.03	8.09E-04	−19.7	0.6	2.64E+10
C.T. Shingletown 1	19	40.50608333	−121.8321944	6.51	9	1.16	0.01	0.25	0.97	0.005			1.50E-03	−15.8	0.6	5.01E+11
Camp Latieze	20	40.45616667	−121.8024167	6.66	12	2.68	0.03	0.35	1.39	0.007	7.04	0.21	1.60E-03	−12.6	0.6	1.64E+11
CAMP-ES-08 - Domestic Well	21	40.3085	−121.7826944	6.59	13	0.99	0.01	0.26	1.03	0.005	0.79	0.02	1.82E-03	−19.2	0.6	5.67E+11
Ponderosa Ranch	22	40.339	−121.7648889	6.61	12.5	1.01	0.01	0.26	1.01	0.005	2.05	0.06	1.87E-03	−18.8	0.6	6.20E+11
BSA Camp Lassen	23	40.55880556	−121.7168889	6.6	8.5	1.38	0.04	0.26	1.03	0.005			1.23E-03			3.30E+11
CAMP-TV-02	24	41.02036111	−121.6806111	7.18	16	1.00	0.01	0.25	1.00	0.005			9.30E-04	−13.4	0.6	3.57E+11
BWD Well #7	25	40.87130556	−121.6603611	7.6	8	1.00	0.01	0.24	0.97	0.005	1.13	0.03	6.00E-04	−18.9	0.6	2.29E+11
Johnson Park Well 1	26	40.91797222	−121.6256944	7.49	10	1.15	0.02	0.26	1.04	0.005	4.62	0.14	6.89E-04			2.09E+11
Butte Meadows	27	40.07894444	−121.5605556	6.8	7.5	1.13	0.01	0.25	1.00	0.005			1.04E-03			3.13E+11
Cassel MWC #1	28	40.91863889	−121.5598056	7.38	11	1.83	0.01	0.30	1.18	0.006	6.53	0.20	9.08E-04	−14.8	0.6	1.49E+11
BSA Camp Lassen	29	40.09422222	−121.5523889	6.6	8.5	1.14	0.01	0.28	1.11	0.006	2.44	0.07	1.47E-03	−21.4	0.6	3.06E+11
USFS WC #1	30	40.80255556	−121.5164722	7.63	13.5	3.94	0.03	0.76	3.00	0.015	5.41	0.16	7.15E-04	−13.5	0.6	2.17E+10
Guernsey Well	31	40.30947222	−121.4263333	8.46	14.5	0.74	0.01	0.40	1.56	0.008	0.28	0.01	4.49E-04	−18.4	0.6	
Chester P.U.D. #3	32	40.29391667	−121.2391389	7.3	8.5	1.32	0.01	0.26	1.04	0.005			9.16E-04	−17.7	0.6	2.09E+11
Chester P.U.D. Well 2	33	40.31386111	−121.2382778	7.1	9	1.72	0.02	0.40	1.58	0.008	2.96	0.09	8.00E-04	−16.5	0.6	8.96E+10
Lake Almanor Well 5	34	40.24225	−121.2073333	7.5	10.5	1.42	0.03	1.59	6.29	0.031	1.50	0.04	1.81E-03	−15.6	0.6	6.29E+10
LVCSD #1	35	40.89322222	−121.1820833	7.51	17.5	0.94	0.01	0.29	1.15	0.006	0.58	0.02	1.15E-03	−14.5	0.6	3.73E+11
Almanor Com 1	36	40.21638889	−121.1714444	6.2	8	1.10	0.03	0.26	1.04	0.005	3.69	0.11	1.76E-03	−20.9	0.6	3.50E+11
Chester R. Stop Well 1	37	40.30263889	−121.1624444	7.98	9.5	1.98	0.02	0.58	2.28	0.011	2.74	0.08	6.57E-04	−16.6	0.6	5.25E+10

For pure fresh water at 10 °C ($\beta Ne/\beta He$) = 1.26 (Weiss, 1971).

[1] $(X)_{fluid} = (^4He/^{20}Ne)_{measured}/(^4He/^{20}Ne)_{air} \times (\beta_{Ne}/\beta_{He})$.

[2] Eq. 2: $R_C/R_A = ((R/R_A \times X) - 1)/(X - 1)$.

[3] Error associated with DIC is 3%.

[4] Error associated with $C/^3He$ is 5%.

Table 2
Modeling outputs and calculations.

Sample	Sample	Csoil.[1]	Cext.[2]	C/^{3}He(app)	^{14}C	$^{14}Cerr$	$^3H(TU)$	Fracfactor(ε).[3]	δ^{13}Csoil. eq.[4]	δ^{13}Cext.[5]	^{3}HeccSTP/gH$_2$O	^{4}HeccSTP/gH$_2$O	^{3}Hecorr	^{4}Hecorr	Rc/Ra(Eq.3)	%mantle^{3}He.[6]	%Crust^{3}He	PANGAatm^{4}He	PANGA^{4}Heerr	^{4}Heexerr	Significantmonatm^{4}He.[7]	PANGAatm^{3}He	TCO_2in(mmol/L).[8]	HCO_3in(mmol/L).[8]	CO_3in(mmol/L).[8]	CO_2in(mmol/L).[8]	HCO_3/DIC	CO_2/DIC
Black Butte JH	1	1.96E-03	2.95E-04	6.82E+10	108.6	0.43	8.2	4.64	−18.36	−45.3	2.01E-13	1.21E-07	9.72E-14	4.65E-08	1.50	18%	82%	7.44E-08	2.47E-09	2.85E-09	significant	1.04E-13	1748.70	939.69	0.39	808.61	0.54	0.46
Ishi Camp Spring	2	1.10E-03	3.09E-04	1.82E+11	78.04	0.26	0.5	8.57	−14.43	−53.0	6.93E-14	5.11E-08	3.81E-14	2.87E-08	0.96	11%	89%	2.25E-08	8.91E-10	9.91E-10	significant	3.14E-14	1322.18	1191.98	4.01	126.19	0.90	0.10
Ponderosa Ranch	3	1.39E-03	4.83E-04	1.46E+11	92.7	0.32	3.4	6.31	−16.69	−59.3	1.43E−13	9.92E-08	7.43E-14	4.98E-08		-1%	101%	4.94E-08	2.67E-07	2.67E-07	insignificant	6.92E-14	1569.72	1088.47	0.88	480.37	0.69	0.31
Shasta Village MWC	4	1.73E-03	5.51E-04	2.36E+11	94.85	0.3	3.8	5.36	−17.64	−34.1	1.31E-13	8.70E-08	5.24E-14	3.02E-08	1.25	15%	85%	5.67E-08	1.45E-09	1.80E-09	significant	7.94E-14	1833.76	1109.14	0.61	724.01	0.61	0.39
Whitmore Union	5	1.49E-03	4.93E-04	1.79E+11	94.01	0.29	1.5	7.18	−15.82	−31.5	1.32E-13	9.03E-08	6.19E-14	3.97E-08	1.12	13%	87%	5.06E-08	8.72E-09	8.79E-09	significant	7.08E-14	1741.21	1346.85	1.65	392.71	0.77	0.23
C.T. Shingletown 1	6	9.24E-04	5.78E-04	1.46E+11	76.88	0.25	11.6	5.77	−17.23	−20.8	1.48E-13	8.74E-08	8.87E-14	4.47E-08	1.43	17%	83%	4.27E-08	2.10E-08	2.11E-08	significant	5.98E-14	1228.31	789.29	0.51	438.52	0.64	0.36
Camp Latieze	7	6.09E-04	9.96E-04	6.88E+10	47.42	0.21	4	6.57	−16.43	−18.2	3.85E-13	1.22E-07	3.25E-13	7.94E-08	2.94	36%	64%	4.31E-08	1.52E-09	1.92E-09	significant	6.03E-14	1364.16	978.43	0.89	384.84	0.72	0.28
Moose Camp	8	6.03E-04	2.06E-04		93.17	0.42	9.2	8.00	−15.00	−36.2	1.57E-13	8.29E-08						5.70E-07	3.39E-08	3.54E-08	insignificant	7.98E-13	739.05	627.52	1.27	110.25	0.85	0.15
BWD Well #7	9	4.33E-04	1.67E-04	5.33E+10	90.21	0.3	6	9.14	−13.86	−38.1	1.31E-13	9.46E-08	7.03E-14	5.06E-08	1.00	12%	88%	4.40E-08	1.79E-08	1.80E-08	significant	6.17E-14	580.45	551.21	4.35	24.89	0.96	0.04
Chester P.U.D. #3	10	7.07E-04	2.09E-04	4.66E+10	96.44	0.33	7.9	8.71	−14.29	−55.0	1.75E-13	9.85E-08	1.01E-13	4.48E-08	1.62	20%	80%	5.37E-08	3.14E-09	3.32E-09	significant	7.52E-14	868.37	793.71	3.14	71.52	0.92	0.08
Guernsey Well	11	2.61E-04	1.89E-04	3.84E+10	58.01	0.24	0.2	9.53	−13.47	−46.6	2.03E-13	1.97E-07	1.10E-13	1.30E-07	0.61	7%	93%	6.64E-08	2.76E-09	3.38E-09	significant	9.29E-14	428.62	403.05	23.05	2.51	0.99	0.01
BSA Camp Lassen	12	1.02E-03	2.12E-04	3.12E+10	103.5	0.33	7.4	6.26	−16.74	−44.4	2.12E-13	1.31E-07	1.52E-13	8.85E-08	1.24	15%	85%	4.30E-08	1.33E-08	1.33E-08	significant	6.02E-14	1029.92	709.12	0.56	320.24	0.69	0.31
Black Butte JH	13	1.96E-03	2.95E-04		108.6	0.43	8.2	4.64	−18.36	−20.9	1.25E-13	7.06E-08						7.44E-08	2.47E-09	2.85E-09	insignificant	1.04E-13	1748.70	939.69	0.39	808.61	0.54	0.46
Whitmore Union	14	1.49E-03	4.93E-04	1.02E+12	94.01	0.29	1.5	7.18	−15.82	−32.1	8.11E−14	5.55E-08	1.08E-14	4.91E-09		-1%	101%	5.06E-08	8.72E-09	8.79E-09	insignificant	7.08E-14	1741.21	1346.85	1.65	392.71	0.77	0.23
Shasta Village MWC	15	1.73E-03	5.51E-04		94.85	0.3	3.8	5.36	−17.64	−30.2	8.03E-14	5.35E-08	1.45E-15					5.67E-08	1.45E-09	1.80E-09	insignificant	7.94E-14	1833.76	1109.14	0.61	724.01	0.61	0.39
Hillcreast SRRA 1	16	1.40E-03	2.22E-04		107.9	0.35	7.4	1.85	−21.15	−17.1	1.12E-13	8.00E-08						8.63E-08	6.97E-09	7.16E-09	insignificant	1.21E-13	1120.52	311.36	0.04	809.12	0.28	0.72
Ishi Camp Spring	17	1.10E-03	3.09E-04		78.04	0.26	0.5	8.57	−14.43	−32.8	2.83E-14	2.17E-08						2.25E-08	8.91E-10	9.91E-10	insignificant	3.14E-14	1322.18	1191.98	4.01	126.19	0.90	0.10
Moose Camp	18	6.03E-04	2.06E-04		93.17	0.42	9.2	8.00	−15.00	−33.6	6.86E-13	5.06E-07						5.70E-07	3.39E-08	3.54E-08	insignificant	7.98E-13	739.05	627.52	1.27	110.25	0.85	0.15
C.T. Shingletown 1	19	9.24E-04	5.78E-04		76.88	0.25	11.6	5.77	−17.23	−13.6	6.72E-14	4.14E-08	7.82E-15					4.27E-08	2.10E-08	2.11E-08	insignificant	5.98E-14	1228.31	789.29	0.51	438.52	0.64	0.36
Camp Latieze	20	6.09E-04	9.96E-04	1.39E+11	47.42	0.21	4	6.57	−16.43	−10.3	2.20E-13	5.85E-08	1.60E-13	1.55E-08	7.44	93%	7%	4.31E-08	1.52E-09	1.92E-09	significant	6.03E-14	1364.16	978.43	0.89	384.84	0.72	0.28
CAMP-ES-08 - Domestic Well	21	1.36E-03	4.60E-04		93.39	0.33	2.7	6.21	−16.79	−26.5	7.20E-14	5.18E-08						5.24E-08	2.00E-09	2.25E-09	insignificant	7.33E-14	1519.42	1038.64	0.80	479.98	0.68	0.32
Ponderosa Ranch	22	1.39E-03	4.83E-04		92.7	0.32	3.4	6.31	−16.69	−24.9	6.77E-14	4.77E-08						4.94E-08	2.67E-07	2.67E-07	insignificant	6.92E-14	1569.72	1088.47	0.88	480.37	0.69	0.31
BSA Camp Lassen	23	0.00E+00					10.6	6.26	−16.74		8.36E-14	4.32E-08	2.38E-14	2.66E-10				4.30E-08	1.33E-08	1.33E-08	insignificant	6.02E-14	1029.92	709.12	0.56	320.24	0.69	0.31
CAMP-TV-02	24	6.46E-04	2.84E-04		86.84	0.31	3.5	8.46	−14.54	−10.8	5.85E-14	4.19E-08						4.36E-08	1.13E-09	1.41E-09	insignificant	6.10E-14	869.80	775.37	2.33	92.10	0.89	0.11

(*continued on next page*)

Table 2 (*continued*)

Sample	Sample	Csoil.[1]	Cext.[2]	C/^{3}He(app)	^{14}C	^{14}Cerr	^{3}H(TU)	Fracfactor(ε).[3]	δ^{13}Csoil, eq.[4]	δ^{13}Cext.[5]	^{3}HeccSTP/gH$_2$O	^{4}HeccSTP/gH$_2$O	^{3}Hecorr	^{4}Hecorr	Rc/Ra(Eq.3)	%mantle^{3}He.[6]	%Crust^{3}He	PANGAatm^{4}He	PANGA^{4}Heerr	^{4}Heexerr	Significantnonatm^{4}He.[7]	PANGAatm^{3}He	TCO$_2$in(mmol/L).[8]	HCO$_3$in(mmol/L).[8]	CO$_3$in(mmol/L).[8]	CO$_2$in(mmol/L).[8]	HCO$_3$/DIC	CO$_2$/DIC
BWD Well #7	25	4.33E-04	1.67E-04		90.21	0.3	6	9.14	−13.86	−31.8	5.89E-14	4.22E-08						4.40E-08	1.79E-08	1.80E-08	insignificant	6.17E-14	580.45	551.21	4.35	24.89	0.96	0.04
Johnson Park Well 1	26	0.00E+00					2	9.01	−13.99		7.37E−14	4.59E-08	1.21E-14	1.58E-09		-1%	101%	4.43E-08	2.21E-08	2.21E-08	insignificant	6.20E-14	662.33	622.31	3.81	36.20	0.95	0.05
Butte Meadows	27	0.00E+00					8.7	7.22	−15.78		7.43E-14	4.68E-08	8.15E-15					4.76E-08	2.88E-09	3.02E-09	insignificant	6.66E-14	911.10	708.37	0.89	201.84	0.78	0.22
Cassel MWC #1	28	6.36E-04	2.72E-04	8.50E+10	87.53	0.29	2.9	8.85	−14.15	−16.4	1.37E−13	5.33E-08	7.18E-14	6.60E-09		-1%	101%	4.67E-08	1.27E-08	1.27E-08	insignificant	6.54E-14	866.29	802.34	3.82	60.13	0.93	0.07
BSA Camp Lassen	29	1.22E-03	2.53E-04	2.90E+11	103.5	0.33	7.4	6.26	−16.74	−43.6	1.08E−13	6.76E-08	1.96E-14	4.03E-09		-1%	101%	6.36E-08	1.99E-09	2.41E-09	insignificant	8.90E-14	1232.93	848.90	0.67	383.36	0.69	0.31
USFS WC #1	30	5.05E-04	2.10E-04	6.98E+09	70.66	0.26	0.5	9.17	−13.83	−12.6	7.37E-13	1.34E-07	6.74E-13	8.83E-08	5.49	68%	32%	4.53E-08	2.00E-09	3.34E-09	significant	6.35E-14	692.09	658.75	5.57	27.76	0.96	0.04
Guernsey Well	31	2.61E-04			58.01	0.24	0.2	9.53	−13.47	−25.1	1.00E-13	9.70E-08	8.19E-15	3.06E-08	0.19	2%	98%	6.64E-08	2.76E-09	3.38E-09	significant	9.29E-14	428.62	403.05	23.05	2.51	0.99	0.01
Chester P.U.D. #3	32	7.07E-04	2.09E-04	1.98E+11	96.44	0.33	7.9	8.71	−14.29	−29.3	9.84E-14	5.32E-08	2.37E-14					5.37E-08	3.14E-09	3.32E-09	insignificant	7.52E-14	868.37	793.71	3.14	71.52	0.92	0.08
Chester P.U.D. Well 2	33	5.34E-04	2.66E-04	4.93E+10	83.39	0.29	7.5	8.26	−14.74	−20.1	2.00E-13	8.32E-08	1.21E-13	2.63E-08	3.31	41%	59%	5.69E-08	9.21E-09	9.36E-09	significant	7.97E-14	740.80	646.81	1.61	92.37	0.88	0.12
Lake Almanor Well 5	34	9.18E-04	8.93E-04	3.52E+10	50.68	0.22	0.3	9.02	−13.98	−17.2	6.46E-13	3.25E-07	5.70E-13	2.70E-07	1.52	18%	82%	5.47E-08	1.25E-08	1.41E-08	significant	7.66E-14	1742.86	1639.38	10.28	93.20	0.95	0.05
LVCSD #1	35	8.84E-04	2.70E-04		76.59	0.26	0.1	9.04	−13.96	−16.1	6.93E-14	5.25E-08	3.08E-15	4.84E-09	0.46	5%	95%	4.76E-08	1.39E-09	1.74E-09	significant	6.67E-14	1111.36	1046.50	6.72	58.14	0.95	0.05
Almanor Com 1	36	1.36E-03	3.97E-04		96.81	0.32	3.7	3.90	−19.10	−27.2	1.13E-13	7.31E-08	9.81E-15					7.40E-08	2.39E-09	2.80E-09	insignificant	1.04E-13	1324.01	620.24	0.19	703.58	0.47	0.53
Chester R. Stop Well 1	37	4.15E-04	2.42E-04	2.48E+10	79.03	0.43	6.9	9.40	−13.60	−21.8	2.81E-13	1.01E-07	2.18E-13	5.62E-08	2.79	35%	65%	4.52E-08	1.23E-08	1.25E-08	significant	6.32E-14	639.66	616.38	11.67	11.60	0.98	0.02

where, $^3He/^4He_{Mantle} = 8\ R_A$, $^3He/^4He_{Crust} = 0.05\ R_A$.

[1] $C_{soil} = (^{14}C_{meas}/^{14}C_{init}) \times DIC$.

[2] Cext = DIC - Csoil; Cext = Cmantle + Cslab.

[3] $\varepsilon = (HCO_3^-/DIC) \times 9.60‰ + (CO_2/DIC) \times -1.13‰$.

[4] $\delta^{13}C_{soil,\ eq} = \delta^{13}C_{soil} + \varepsilon$. $\delta^{13}C_{soil}$ is assumed to be −23‰.

[5] δ13Cext = (δ13Cmeas - (Csoil/DIC) × δ13Csoil, eq)/(Cext/DIC).

[6] % mantle 3He = $(R_C/R_A - {}^3He/^4He_{Crust}) / (^3He/^4He_{Mantle} - {}^3He/^4He_{Crust})$.

[7] Helium in exess of air and excess air at the 95% confidence interval.

[8] Outputs from CO2SYS software.

Table 3
Volatile source estimates.

Sample	Sample #	%C derived from mantle[1]	Cext (mol/L)	Cmantle (mol/L)	Cslab (mol/L)	%Csoil of DIC	%Cext of DIC	%Cext derived from mantle	%slab of EXT	$\delta^{13}C$ slab[2]	Fsediment[3]	Flimestone[4]	$CO_2/^3He$ ext[5]	f[6]
Black Butte JH	1	0.38%	2.95E-04	8.67E-06	2.87E-04	86.9%	13.1%	2.9%	97%	−46.5	1.16	−0.16	6.82E+10	0.99
Ishi Camp Spring	2	0.24%	3.09E-04	3.40E-06	3.05E-04	78.0%	22.0%	1.1%	99%	−53.5	1.34	−0.34	1.82E+11	1.00
Ponderosa Ranch	3	0.35%	4.83E-04	6.63E-06	4.76E-04	74.2%	25.8%	1.4%	99%	−60.1	1.50	−0.50	1.46E+11	1.00
Shasta Village MWC	4	0.20%	5.51E-04	4.67E-06	5.46E-04	75.9%	24.1%	0.8%	99%	−34.3	0.86	0.14	2.36E+11	0.96
Whitmore Union	5	0.28%	4.93E-04	5.52E-06	4.87E-04	75.2%	24.8%	1.1%	99%	−31.8	0.79	0.21	1.79E+11	0.94
C.T. Shingletown 1	6	0.53%	5.78E-04	7.91E-06	5.70E-04	61.5%	38.5%	1.4%	99%	−21.0	0.53	0.47	1.46E+11	0.75
Camp Latieze	7	1.81%	9.96E-04	2.90E-05	9.67E-04	37.9%	62.1%	2.9%	97%	−18.5	0.46	0.54	6.88E+10	0.65
Moose Camp	8		2.06E-04	0.00E+00	2.06E-04	74.5%	25.5%				0.00			0.97
BWD Well #7	9	1.04%	1.67E-04	6.27E-06	1.61E-04	72.2%	27.8%	3.8%	96%	−39.4	0.98	0.02	5.33E+10	0.97
Chester P.U.D. #3	10	0.98%	2.09E-04	8.99E-06	2.00E-04	77.2%	22.8%	4.3%	96%	−57.3	1.43	−0.43	4.66E+10	1.00
Guernsey Well	11	2.19%	1.89E-04	9.84E-06	1.79E-04	58.0%	42.0%	5.2%	95%	−48.9	1.22	−0.22	3.84E+10	0.99
BSA Camp Lassen	12	1.10%	2.12E-04	1.36E-05	1.98E-04	82.8%	17.2%	6.4%	94%	−47.1	1.18	−0.18	3.12E+10	0.99
Black Butte JH	13		2.95E-04	0.00E+00	2.95E-04	86.9%	13.1%				0.00	1.00		0.76
Whitmore Union	14	0.05%	4.93E-04	9.62E-07	4.92E-04	75.2%	24.8%	0.2%	100%	−32.1	0.80	0.20	1.02E+12	0.94
Shasta Village MWC	15		5.51E-04		5.51E-04	75.9%	24.1%		100%	−30.2	0.76	0.24	8.50E+12	0.93
Hillcreast SRRA 1	16		2.22E-04		2.22E-04	86.3%	13.7%		100%	−17.1	0.43	0.57		0.60
Ishi Camp Spring	17		3.09E-04		3.09E-04	78.0%	22.0%		100%	−32.8	0.82	0.18		0.95
Moose Camp	18		2.06E-04		2.06E-04	74.5%	25.5%		100%	−33.6	0.84	0.16		0.95
C.T. Shingletown 1	19		5.78E-04		5.78E-04	61.5%	38.5%		100%	−13.6	0.34	0.66	1.66E+12	0.37
Camp Latieze	20	0.89%	9.96E-04	1.43E-05	9.82E-04	37.9%	62.1%	1.4%	99%	−10.3	0.26	0.74	1.39E+11	0.03
CAMP-ES-08 - Domestic Well	21		4.60E-04		4.60E-04	74.7%	25.3%		100%	−26.5	0.66	0.34		0.88
Ponderosa Ranch	22		4.83E-04		4.83E-04	74.2%	25.8%		100%	−24.9	0.62	0.38		0.86
BSA Camp Lassen	23	0.17%		2.13E-06	−2.13E-06				100%		0.00			
CAMP-TV-02	24		2.84E-04		2.84E-04	69.5%	30.5%		100%	−10.8	0.27	0.73		0.10
BWD Well #7	25		1.67E-04		1.67E-04	72.2%	27.8%		100%	−31.8	0.79	0.21		0.94
Johnson Park Well 1	26	0.16%		1.08E-06	−1.08E-06				100%		0.00			
Butte Meadows	27				0.00E+00				100%		0.00			
Cassel MWC #1	28	0.71%	2.72E-04	6.40E-06	2.66E-04	70.0%	30.0%	2.4%	98%	−16.7	0.42	0.58	8.50E+10	0.57
BSA Camp Lassen	29	0.12%	2.53E-04	1.75E-06	2.51E-04	82.8%	17.2%	0.7%	99%	−43.8	1.10	−0.10	2.90E+11	0.99
USFS WC #1	30	8.41%	2.10E-04	6.01E-05	1.50E-04	70.7%	29.3%	28.7%	71%	−15.7	0.39	0.61	6.98E+09	0.29
Guernsey Well	31				0.00E+00	58.0%			100%		0.00			
Chester P.U.D. #3	32	0.23%	2.09E-04	2.11E-06	2.07E-04	77.2%	22.8%	1.0%	99%	−29.6	0.74	0.26	1.98E+11	0.92
Chester P.U.D. Well 2	33	1.35%	2.66E-04	1.08E-05	2.56E-04	66.7%	33.3%	4.1%	96%	−20.7	0.52	0.48	4.93E+10	0.73
Lake Almanor Well 5	34	2.80%	8.93E-04	5.08E-05	8.42E-04	50.7%	49.3%	5.7%	94%	−18.0	0.45	0.55	3.52E+10	0.61
LVCSD #1	35		2.70E-04		2.70E-04	76.6%	23.4%		100%	−16.1	0.40	0.60	1.97E+12	0.55
Almanor Com 1	36		3.97E-04		3.97E-04	77.4%	22.6%		100%	−27.2	0.68	0.32	9.08E+11	0.89
Chester R. Stop Well 1	37	2.96%	2.42E-04	1.95E-05	2.22E-04	63.2%	36.8%	8.1%	92%	−23.3	0.58	0.42	2.48E+10	0.78

[1] Cmantle = (^{3}Heexcess) × (C/^{3}Hemantle).
[2] δ^{13}Cslab = δ^{13}Cext – (δ^{13}Cmantle Fmantle / (1 - Fmantle).
[3] Fsediment = (δ^{13}Cslab - δ^{13}Climestone)/ (δ^{13}Csediment - δ^{13}Climestone).
[4] 1-Fsediment.
[5] $CO_2/^3He$ ext. = $C_{ext}/^3He_{corr}$.
[6] f = 1-[(Exp(Ln((δ^{13}Cext +1000)/(δ^{13}Cext-init +1000))/(α-1)))]. α = Exp((= − 8.914 × $10^8/T^3$ + 8.557 × $10^6/T^2$ - 18.11 × $10^3/T$ +8.27)/1000).

Table 4
Water chemistry data.

Date Sampled	Well ID	Well Name	TDS (mg/L)	SC[1]	pH	Temp (°C)	alk[2] (mg/L)	Ca (mg/L)	Mg (mg/L)	K (mg/L)	Na (mg/L)	Cl (mg/L)	SO4 (mg/L)	Br (mg/L)	Nitrate (mg/L)	$\delta^{18}O$ (permil)	δD (permil)	Well Depth (m)	Top of perf (m)	Bottom of perf (m)	Cations (meg/L)	Anions (meg/L)	Ionic balance
14-09-2010	CAMP-ES-03	Ishi Camp Spring	172.67	224.5	7.23	19	120.2	17.82	12.97	1.631	11.35	0.965	1.046	0.01	0.265	−10.72	−77.2				2.49	2.46	TRUE
21-09-2010	CAMP-ES-07	Ponderosa Ranch	171.14	206.5	6.61	12.5	108.8	20.65	10.37	1.932	7.426	1.027	1.285	0.02	0.068	−11.32	−81.3	24.4	24.4	18.3	2.26	2.23	TRUE
04-10-2010	CAMP-ES-08	Domestic Well	152.49	196.9	6.59	13	104.4	17.19	10.68	1.845	7.922	1.028	0.569	0.01	0.092	−11.54	−81	118.9	117.7	105.5	2.13	2.13	TRUE
30-08-2010	CAMP-LU-14	Chester P.U.D. Well 2	77.06	115	7.1	9	64.64	7.696	6.117	2.642	6.156	0.493	0.459	0.02	0.059	−13.48	−97.1	71.6	71.6	49.4	1.22	1.32	FALSE
30-08-2010	CAMP-LU-14	Chester P.U.D. Well 2	77.06	115	7.1	9	64.64	7.696	6.117	2.642	6.156	0.493	0.459	0.02	0.059	−13.48	−97.1	71.6	71.6	49.4	1.22	1.32	FALSE
30-08-2010	CAMP-LU-15	Chester P.U.D. #3	107.56	156	7.3	8.5	80.25	16.43	6.717	2.123	5.627	1.436	0.569	0.0145	0.432	−13.62	−99.7	113.1	113.1	69.5	1.67	1.66	TRUE
09-08-2010	CAMP-QV-05	Johnson Park Well 1	84.28	125.3	7.49	10	63.08	10.06	5.881	1.744	5.348	0.545	0.364	0.02	0.107	−12.76	−91.6	68.9	68.9	68.9	1.26	1.29	TRUE
17-08-2010	CAMP-QV-07	BWD Well #7	71.11	107.5	7.6	8	56.49	9.076	4.796	1.441	3.863	0.254	0.18	0.02	0.059	−12.64	−89.7	91.4	91.4	76.2	1.05	1.14	FALSE
17-08-2010	CAMP-QV-08	Cassel MWC #1	120.87	161.6	7.38	11	80.57	11.65	7.748	2.563	7.892	1.281	2.104	0.02	0.227	−13.81	−99.8	76.2	74.4	56.1	1.63	1.69	FALSE
13-09-2010	CAMP-QV-10	Whitmore Union	182.9	246.6	6.79	14	135.2	21.08	16.13	0.665	6.506	0.89	0.306	0.02	0.072	−10.98	−80.4	53.0	53.0	14.3	2.68	2.74	TRUE
13-09-2010	CAMP-QV-11	Shasta Village MWC	166.02	208.3	6.44	10.5	110.7	22.24	10.45	0.656	5.698	1.142	0.427	0.02	0.168	−11.36	−78.4	51.8	51.8	33.5	2.23	2.26	TRUE
14-09-2010	CAMP-QV-12	Black Butte	149.04	177.6	6.32	12	94.3	15.81	11.01	0.329	4.381	1.048	0.316	0.02	0.07	−10.95	−77.6	70.7	70.7	0.9	1.89	1.92	TRUE
14-09-2010	CAMP-QV − 13	Camp Latieze	150.4	189.1	6.66	12	98.39	12.08	10.39	3.024	10.26	1	2.475	0.02	0.073	-13	−93.5	57.0	56.1	50.0	1.98	2.05	FALSE
15-09-2010	CAMP-QV-14	Guernsey Well	94.87	86.4	8.46	14.5	44.57	1.786	1.244	1.993	14.82	0.681	0.453	0.02	0.031	−13.65	−99.2	141.7	141.7	73.2	0.89	0.92	FALSE
20-09-2010	CAMP-QV-15	C.T. Shingletown 1	116.59	154.7	6.51	9	78.95	11.55	7.563	2.277	8.632	0.799	2.127	0.02	0.177	−12.41	−88				1.63	1.65	TRUE
04-08-2010	CAMP-TV-02	CAMP-TV-02	114.5	156.3	7.18	16	77.51	10.6	6.825	2.417	11.79	2.952	2.326	0.0131	0.229	−13.11	−97.6				1.67	1.69	TRUE
16-08-2010	CAMP-TV-04	USFS WC #1	111.71	139.6	7.63	13.5	66.88	7.692	5.85	2.518	9.904	3.137	1.083	0.0138	0.091	−13.49	−94.6		91.4		1.36	1.45	FALSE
16-08-2010	CAMP-TV-05	LVCSD #1	164.15	209.1	7.51	17.5	106.4	12.7	9.999	4.475	12.5	2.214	0.602	0.0142	0.441	−14.23	−108.6	91.4	91.4	64.0	2.11	2.21	FALSE
25-08-2010	CAMP-TV-06	Chester R. Stop Well 1	85.14	121.1	7.98	9.5	64.29	10.68	6.061	1.757	4.213	0.57	0.178	0.02	0.1	−14.01	−101				1.26	1.31	FALSE
02-09-2010	CAMP-TV-09	Lake Almanor Well 5	190.59	311	7.5	10.5	166.4	24.3	22.11	1.968	7.675	6.321	2.01	0.0213	0.06	−13.79	−100.2	125.0	122.8	48.2	3.41	3.55	FALSE
02-09-2010	CAMP-TV-10	Almanor Com 1	80.28	116.3	6.2	8	62.07	10.15	7.069	0.882	2.345	0.734	0.18	0.02	0.398	−13.42	−97.3	91.4	91.4		1.21	1.27	FALSE
15-09-2010	CAMP-TV-11	Moose Camp	93.93	121.5	7.01	8	63.07	11.66	6.977	0.353	2.284	0.294	0.18	0.02	0.586	−11.43	−80	61.6			1.26	1.28	TRUE
15-09-2010	CAMP-TV-12	Butte Meadows	97.63	133.2	6.8	7.5	70.73	12.61	7.125	1.161	4.022	0.659	0.223	0.02	0.086	−11.35	−79.3	64.0	64.0	51.8	1.42	1.44	TRUE
16-09-2010	CAMP-TV-13	BSA Camp Lassen	117.71	157.1	6.6	8.5	84.99	13.99	9.455	1.15	3.561	0.496	0.138	0.02	0.077	−11.24	−78.9	41.1			1.66	1.72	FALSE
21-09-2010	CAMP-TV-14	Hillcreast SRRA 1	53.92	63.9	5.84	10	30.74	3.777	4.728	0.148	1.002	0.42	0.143	0.02	0.646	−10.86	−75	53.3	53.3	47.2	0.62	0.64	TRUE

[1] microsiemens per centimeter at 25 degrees Celsius.
[2] Alkalinity, water, filtered, fixed endpoint (pH 4.5) titration.

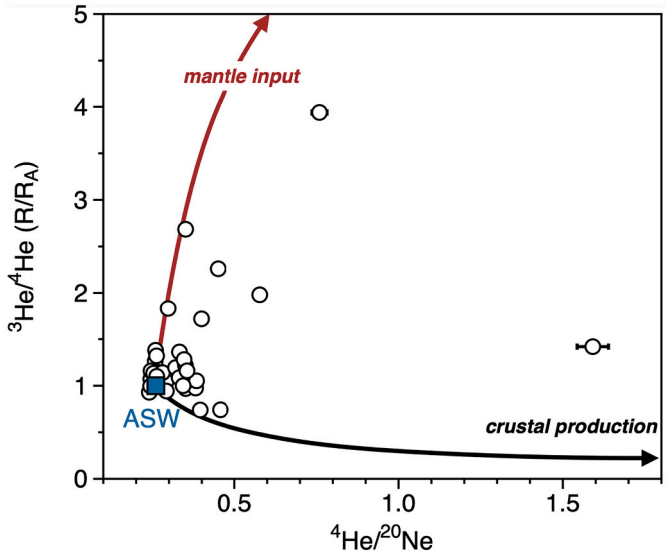

Fig. 2. Measured He isotopes ($^3He/^4He$) vs. $^4He/^{20}Ne$, with binary mixing trajectories between air-saturated water (ASW) and mid-ocean ridge basalt (MORB-like) mantle and crust superimposed. Binary mixing lines are calculated using assumed endmembers of: ASW $^3He/^4He = 1$ R$_A$, $^4He/^{20}Ne = 0.26$ (at 10 °C) (Ozima and Podosek, 2002), MORB $^3He/^4He = 8$ R$_A$, $^4He/^{20}Ne = 2{,}000$ (Graham, 2002), crustal $^3He/^4He = 0.05$ R$_A$, and $^4He/^{20}Ne = 2{,}000$ (Morrison and Pine, 1955). Notably, all samples have higher $^4He/^{20}Ne$ than air, so He—Ne cannot be explained by excess air. Instead, all data require a three-component mixture of ASW-Crust-Mantle.

gas abundances were determined. An aliquot of purified He and Ne was then collected in a 1720-glass breakseal for analysis on a separate line. An aliquot of CO_2 was taken by heating the CO_2 on the U-tube to room temperature, and transferring it to a Pyrex® glass breakseal for C isotope analysis.

The CO_2 in the glass breakseal was then inlet into a dedicated CO_2 clean up line to quantify the total amount of CO_2 in the sample and to remove any other interfering gas species (e.g., H_2S) before being transferred to an isotope-ratio mass spectrometer. Purification was accomplished by freezing the gas onto a variable-temperature trap, where the temperature was slowly raised from −196 °C to −140 °C, allowing the CO_2 to be released, while any interfering species remained frozen. This purified CO_2 was then manometrically measured using a Baratron®. CO_2 was finally transferred to a collection finger, where it was again frozen at liquid nitrogen temperature for transfer to an isotope ratio mass spectrometer (IRMS). The Baratron® pressure was used to calculate the total amount of CO_2 in each sample.

3.3. Dynamic IRMS (Thermo Finnigan DELTAplus XP)

CO_2 aliquots were inlet into a Thermo Finnigan DELTAplus XP isotope-ratio mass spectrometer (IRMS) at SIO to measure $\delta^{13}C$. Depending on the amount of CO_2 in the breakseal, two methods were used to measure the $\delta^{13}C$ ratio: the He carrier method and the dual inlet method (Barry et al., 2014). Using the He carrier method, the glass sample container was cracked and the sample was carried into the IRMS by He gas. With the dual inlet method, the breakseal was cracked and the CO_2 was transferred to a bellows, with a second bellows holding a standard of known isotopic composition. Through a series of valves, the sample and standard were alternately inlet into the IRMS for measurement. The dual inlet method is favored for larger volume samples that have enough gas to make multiple measurements, whereas the helium carrier method is preferable for lower concentration samples. The dual inlet method is more precise (1 sigma error ~ 0.1‰) as it measures the gas multiple times compared to the helium carrier (~0.6‰). All measurements are compared to a Vienna Pee Dee Belemnite (VPDB) standard. Reported uncertainties are the standard deviations from the sample and standard measurements combined.

3.4. Accelerator Mass Spectrometry (NOSAMS)

All samples were measured for $\delta^{13}C$ of dissolved inorganic carbon in water and ^{14}C abundances using the accelerator mass spectrometry at Woods Hole Oceanographic Institution (WHOI), National Ocean Sciences Accelerator Mass Spectrometry (NOSAMS) Facility, following the methods of McNichol et al., 1994. Radiocarbon data from duplicate samples were used to model SIO data.

3.5. Static Mass Spectrometry (SIO)

Helium isotopes (^3He, ^4He) and ^{20}Ne were measured on a Mass Analyzer Products (MAP) 215 noble gas mass spectrometer. Breakseals from the gas extraction line were transferred to the gas cleanup section of the MAP line. Gas samples were released and purified using a charcoal finger (−196 °C) and a titanium getter (700 °C) to remove any remaining argon or reactive gas species. Then, He and Ne were frozen onto a cryogenic trap at 15 K and sequentially released by raising the temperature to 35 K to facilitate He release prior to inlet into the mass-

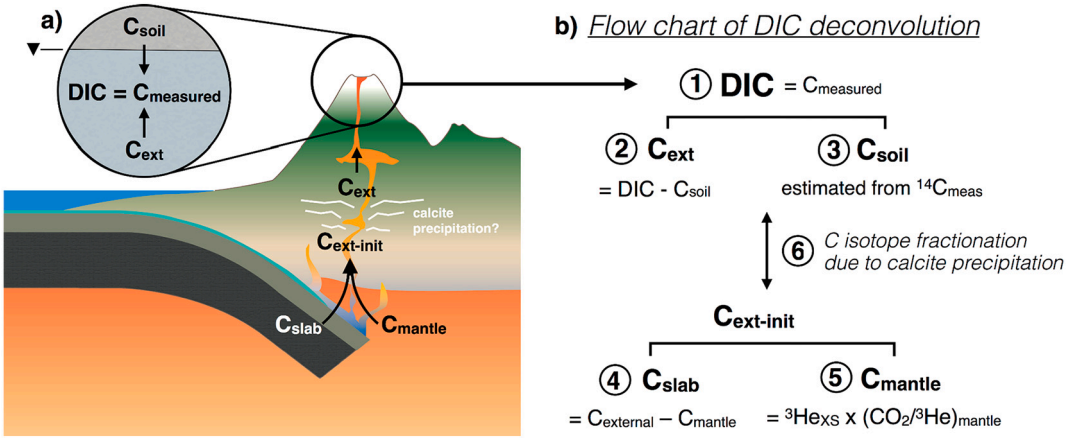

Fig. 3. Left panel: Cartoon showing the various carbon sources in subduction-influenced volcanic systems. DIC contents and C isotopes are measured in fluid samples. Using ^{14}C data, DIC can be subdivided into C derived from soil CO_2 dissolution and C derived from an external (deep) source. We propose a model whereby the apparent external carbon is actually the fractionated remnant from an initial external carbon pool derived from slab and mantle contributions. Right panel: Flow chart showing steps 1–6 as to how the C pools are deconvoluted.

spectrometer. In the MAP 215, ^{3}He was measured by a continuous dynode electron multiplier, while ^{4}He was measured on a Faraday cup. The cryogenic trap was then raised to 90 K to release Ne, which was also measured on a Faraday cup. Helium ratios are reported relative to the ^{3}He/^{4}He of air ($R_A = 1.39 \times 10^{-6}$). Aliquots of an air standard were run between each analysis for direct comparison with our samples (Kulongoski et al., 2003).

3.6. Quadrupole Mass Spectrometry (LLNL)

On all samples, dissolved noble gases and tritium were measured by the ^{3}He in-growth and mass spectrometry at Lawrence Livermore National Laboratory following the methods of Visser et al., 2012. Specifically, a Noble Gas Membrane Inlet Mass Spectrometry (NG-MIMS) system was used to measure noble gases at natural abundances in the Lassen groundwater samples. The NG-MIMS system is equipped with a membrane inlet, a water trap, a CO_2 trap, two getters and a quadrupole mass spectrometer, with an electron multiplier (Visser et al., 2013). The full suite of noble gases isotopes He, Ne, Ar, Kr and Xe are measured every 10 s. The full suite of noble gas data from LLNL samples were used to correct SIO helium isotope data (Section 5.1), since only He and Ne isotopes were measured at SIO.

4. Results

Helium (^{3}He/^{4}He) and C isotope ratios and ^{4}He/^{20}Ne (Fig. 2), and total abundances are reported in Tables 1 and 2. Major ion water chemistry is presented in Table 4.

4.1. Helium isotopes (^{3}He/^{4}He)

Helium isotope data (^{3}He/^{4}He of sample = R) are reported relative to air (R_A) and corrected (R_C/R_A) for blank (consistently less than 1%) and air contributions. Measured ^{3}He/^{4}He values (R/R_A) range from 0.74 to 3.94 R_A (Fig. 2). Two approaches are used to estimate air contributions and apply a correction. Details of this correction are described using eqs. 1–3 in section 5.1. Once air corrections have been applied, we can assess relative contributions of mantle and crustal He to the system. Most samples are dominated by radiogenic He, but all have quantifiable mantle contributions. Several samples have clear ^{3}He/^{4}He (R/R_A) anomalies (Fig. 2), which become even more apparent when air corrections are applied. Across the Lassen region, air corrected He isotope ratios (R_C/R_A) range from 0.19 R_A to 7.44 R_A (Table 2) and agreement between the two correction methods is excellent ($R^2 = 0.972$; Fig. S1). Air corrected He isotope values are generally overlapping or lower (i.e., more radiogenic) than reports of He isotopes (up to 7.3 R_A) from the Lassen volcanic setting (Craig et al., 1978; Welhan et al., 1988). The highest values fall just within nominal range of values associated with upper mantle He (8 ± 1 R_A; Graham, 2002) and above the mean He isotope value for arc gases of ~5.4 R_A (Hilton et al., 2002). Notably, the lowest values reported here in Lassen samples are approaching the radiogenic He production ratio of 0.05 R_A (Morrison and Pine, 1955).

4.2. Carbon isotopes ($\delta^{13}C$ of CO_2) and ^{14}C activities

Measured C-isotopes (δ^{13}C) range from −12.6 to −27.7‰ (versus VPDB) and data from WHOI and SIO is in good agreement (Table 1). Blank contributions were consistently lower than 1%. Radiocarbon (^{14}C) activities range from 47.4 to 108.6% modern carbon (pmc). Several conceptual carbon isotope mixing and fractionation models are discussed in detail in sections 5.2 and 5.3.

4.3. C/^{3}He values

The C/^{3}He were calculated by combining ^{3}He contents with DIC measurements. Ratios vary by approximately two orders of magnitude in Lassen samples, from ~2.2×10^{10} up to ~1.1×10^{12}, all of which are well above the typical MORB value (~2×10^9) and in the range of crustal endmembers (1×10^{11} to 1×10^{13}; O'nions and Oxburgh, 1988).

5. Discussion

Various sources and secondary processes can affect regional groundwater He–CO_2 characteristics. In section 5.1, we discuss the origin of He dissolved in groundwater samples, regional He variations and geological and hydrological controls. Using air-corrected He isotope ratios (determined using two independent approaches; eqs. 1–3), we show that mantle He contributions can be resolved (average = ~19%; Table 2). In section 5.2, we use C/^{3}He and δ^{13}C data to explore several conceptual models that can be used to explain deep (i.e., external) C source signals and possible secondary processes (e.g., shallow carbonate loss) occurring in the crust. In these conceptual models, once external C contributions are deconvolved from soil-derived CO_2, the carbon pools can be further subdivided into mantle vs. non-mantle (i.e., slab derived) contributions using C/^{3}He. We show, using a mass balance approach, that mantle C contributions to the external C pool must be small

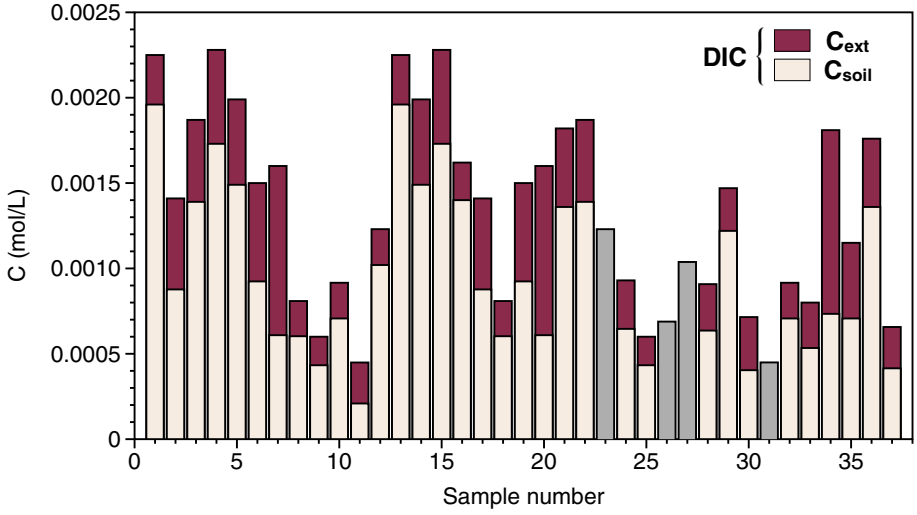

Fig. 4. Bar graph showing the breakdown of DIC into: C_{soil} vs C_{ext}. Sample numbers correspond to those in Fig. 1 and in the tables. For the four samples that cannot be split into C_{soil} vs C_{ext} (because there is either no He data or no ^{14}C data), total DIC is shown as grey bars.

(average ~ 4.2%). Assuming non-mantle C is solely slab-derived, we use C isotopes to explore mixing models whereby slab components are deconvolved into organic sediment vs. limestone contributions (using the methods of Sano and Marty, 1995). Due to extremely light $\delta^{13}C$ (<−29‰ on average) following soil CO_2 correction, we suggest that the vast majority of C must be derived from organic carbon in sediments in a simple mixing scenario. However, this approach requires an unrealistically light organic sediment endmember ($\delta^{13}C$ of ~ −60‰) for the most extremely depleted samples, suggesting that simple mixing is in fact not valid and additional processes must be affecting the carbon isotopes of the system. In section 5.3, we present an idealized calcite fractionation model that could conceivably account for the observed isotopically light $\delta^{13}C$. Finally, a maximum plausible estimate of passive external (slab and mantle) flux of C – dissolved in groundwaters – is calculated (section 5.4) and compared to geothermal C fluxes and regional soil gas C fluxes.

5.1. Helium sources

At face value, several of the measured He isotope (R/R_A) values appear air-like (=1 R_A). However, the vast majority (i.e., 32 out of 37) of samples have clear $^4He/^{20}Ne$ excesses relative to ASW $^4He/^{20}Ne$ (=0.26 at 10 °C; Fig. 2). In contrast to studies in which $^4He/^{20}Ne$ exceeds ASW values by orders of magnitude, these groundwater samples thus have relatively small excess ^4He abundances. We therefore only correct (n = 17) those samples which have statistically significant excess ^4He using Eq. 3 (i.e., samples with an excess of modeled ^4He at 95% confidence, using the CE model constrained by Ne, Ar, Kr, and Xe measured in each well). As noted below, we adopt two approaches to correct helium isotope ratios (see Eq. 2 and Eq. 3 below) for the influence of atmospheric additions, and there is excellent agreement ($R^2 = 0.972$; Fig. S1) between air-corrected helium isotope ratios (R_C/R_A). The first approach follows the methods of Hilton (1996) and uses only the $^4He/^{20}Ne$, assuming no excess air. The second approach employs the CE model (Aeschbach-Hertig et al., 2000), constrained by Ne, Ar, Kr, and Xe, to quantitatively determine air-derived ^3He and ^4He, such that R_c/R_A is calculated by subtracting air-derived helium isotope abundances from measured helium isotopes.

In the first approach, measured $^4He/^{20}Ne$ values are converted into X values using temperature-dependent Bunsen solubility coefficients (β;

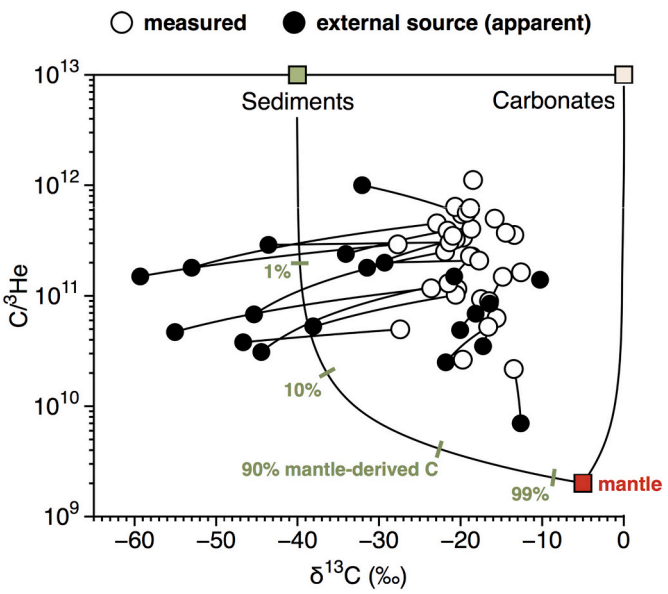

Fig. 6. $C/^3He$ vs. $\delta^{13}CO_2$. Open symbols are measured values and closed (black) symbols are corrected for soil CO_2, $\delta^{13}C$ (Eq. 9) and air derived ^3He. Tie-lines are shown connecting measured and corrected values. Subduction-related source end-member compositions for mantle (= red square; $\delta^{13} = -5‰$; $C/^3He = 2 \times 10^9$), limestone (= beige square; $\delta^{13} = 0‰$; $C/^3He = 1 \times 10^{13}$), and sediment (= green square; $\delta^{13} = -40‰$; $C/^3He = 1 \times 10^{13}$) are given along with mixing lines, after Sano and Marty (1995). Mixing lines (with ticks to show % mantle C) represent binary mixtures between the three endmember values. The uncertainties on the $C/^3He$ vs. $\delta^{13}CO_2$ data are smaller than the size of the symbols. Only a fraction of this data can be explained by a three-component mixture between mantle and subduction related components (i.e., limestone and sediments). Mixing scenarios require an extremely light sediment component, well below accepted values, which are closer to ~ −20‰. (For interpretation of the references to color in this figure legend, the reader is referred to the web version of this article.)

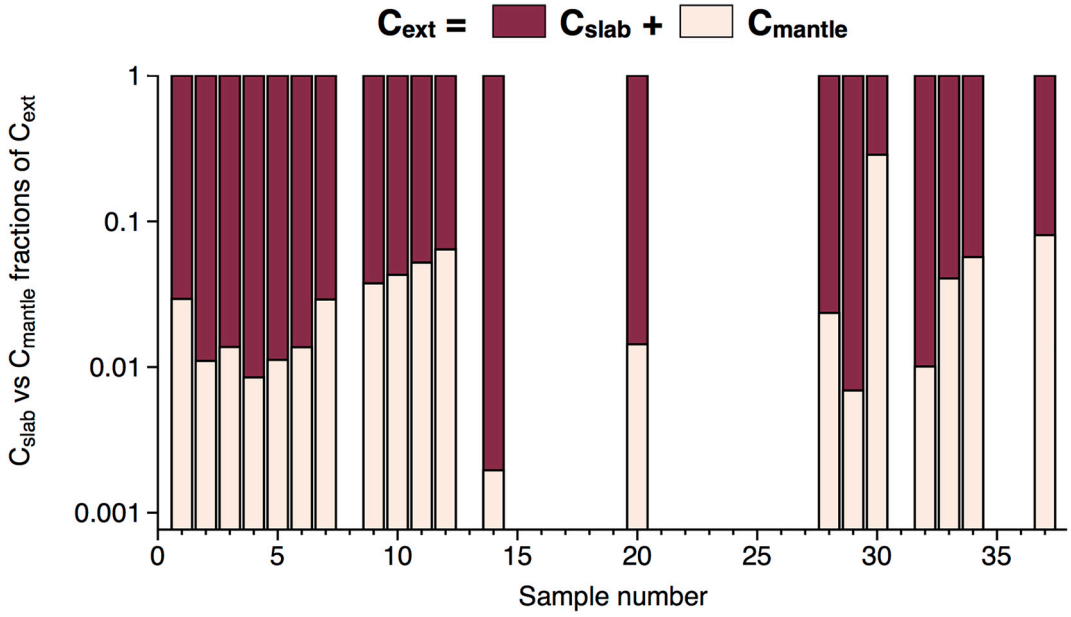

Fig. 5. Bar graph showing the breakdown of C_{ext} into C_{slab} vs C_{mantle}. The y-axis (C (mmol/L) is a log scale, meaning the external carbon pool is strongly dominated by non-mantle contributions, which we consider to be slab-derived in our model. Samples without values did not have statistically significant excess ^3He at the 95% confidence interval, so the calculation was not made.

Weiss, 1971):

$$(X)_{fluid} = \left(^4He/^{20}Ne\right)_{measured} \Big/ \left(^4He/^{20}Ne\right)_{air} \times (\beta_{Ne}/\beta_{He}) \quad (1)$$

For pure fresh water at 10 °C (β_{Ne}/β_{He}) = 1.26 (Weiss, 1971). $(^4He/^{20}Ne)_{measured}$ is the measured ratio in the sample and $(^4He/^{20}Ne)_{air}$ is the measured value in air.

Again, following the methods of Hilton (1996), X can then be combined with measured He isotope values (R/R_A) to calculate a corrected He isotope value (R_C/R_A):

$$R_C/R_A = ((R/R_A \times X)-1)/(X-1) \quad (2)$$

Where R/R_A = the measured He isotope value, reported relative to air ($=1.39 \times 10^{-6}$) and X is calculated using eq. 1. Notably however, this approach breaks down when the X-value is very close to 1, resulting in unrealistically large corrections, thus the second approach below is preferable for the Lassen region samples.

The second approach to calculate R_C/R_A is using the following equation:

$$R_C/R_A = \left(\left(^3He_{meas}-^3He_{ASW}-^3He_{EA}\right)/\left(^4He_{meas}-^4He_{ASW}-^4He_{EA}\right)\right) / \left(1.39 \times 10^{-6}\right) \quad (3)$$

This approach requires knowledge of both ASW concentrations and excess air (EA) in the system (Heaton and Vogel, 1981; Aeschbach-Hertig and Solomon, 2013). If a full suite of noble gas data (e.g., Ne, Ar, Kr, Xe) is available, both parameters can be estimated using the CE model (Aeschbach-Hertig et al., 2000). For implementation of the CE model, we assume that recharge elevation is equal to well elevation. Samples without a full suite of noble gases available (SIO samples) were assumed to have identical ASW concentrations and excess air (EA) as duplicate (NOSAMS) samples from the same wells.

We note that the difference in the solutions given by eqs. (2,3) are negligible for water samples with high $^4He/^{20}Ne$ values. However, in Lassen region groundwater samples, many measured $^4He/^{20}Ne$ values are on the same order of magnitude as ASW, clearly indicating a non-negligible excess air influence on He. We therefore adopt the excess-air approach (Eq. 3) to calculate R_C/R_A for all samples in this study (Table 2), however we note that the agreement between the two methods is excellent (R^2 = 0.972; Fig. S1). Once air contributions are quantified and corrected for, we use air-corrected He isotope (R_C/R_A) values to calculate the fraction of mantle-derived He, assuming a binary mixture between mantle and crustal endmembers (e.g., Barry et al., 2013):

$$\%\text{Mantle He} = \left(R_C/R_A - ^3He/^4He_{Crust}\right)/\left(^3He/^4He_{Mantle} - ^3He/^4He_{Crust}\right) \quad (4)$$

where, $^3He/^4He_{Mantle}$ = 8 R_A, $^3He/^4He_{Crust}$ = 0.05 R_A (Graham, 2002; Morrison and Pine, 1955).

The extent of mixing between air, crustal and mantle components is likely controlled by the complex geology and associated groundwater flow paths in the region. As noted above, $^3He/^4He$ and $^4He/^{20}Ne$ vary from well to well (Fig. 2). In general, samples that plot close to 1 R_A have low $^4He/^{20}Ne$ values, whereas samples with the lowest (Guernsey Well) and highest He isotope values (i.e., Camp Latieze, USFS WC #1) have amongst the highest $^4He/^{20}Ne$ values (Fig. 2). The highest He isotope value measured (at Camp Latieze) is within the upper mantle He range (8 ± 1 R_A; Graham, 2002) and nearly identical to the highest He isotope values (~7.3 R_A) every reported from the Lassen volcanic setting (Craig et al., 1978; Welhan et al., 1988). The second highest value measured (at USFS WC #1) is nearly identical to the mean He isotope value for arc gases (~5.4 R_A; Hilton et al., 2002). These two samples have the highest % mantle ^3He, as calculated in Eq. 4 and tabulated in Table 2.

Other explanations for high $^3He/^4He$ including radioelement heterogeneity, high lithium content, or the preferential release of ^3He from the aquifer matrix (Kulongoski et al., 2003) have not been identified in the Lassen Peak region and are assumed to be insignificant. High nuclear bomb-tritiated water also may generate ^3He, but contributions of bomb-^3He calculated from the decay of peak tritium levels in the 1960s to current tritium values, and impacts on percent mantle helium calculations, are insignificant given the high $^3He/^4He$ ratios measured.

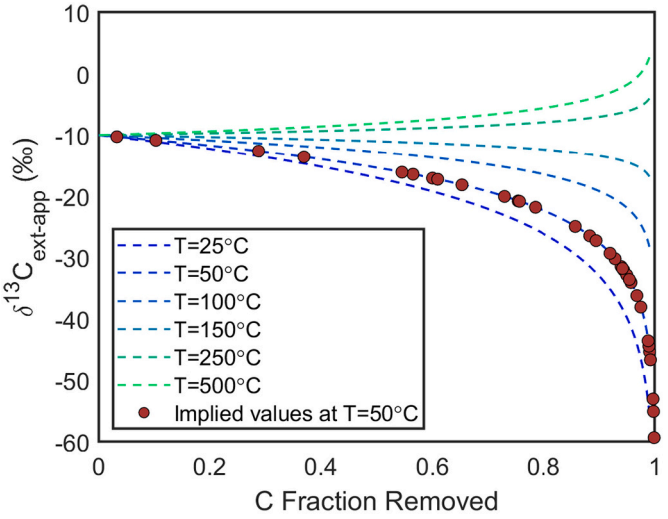

Fig. 7. Predictions of the fraction (f) of C that must have been removed (Eq. 18) from the fluids due to calcite precipitation, assuming a starting slab C isotope composition of − 10‰. Apparent external C isotope values are calculated using Eq. 9, using measured C isotope values and estimates of soil CO_2 contributions from measured ^{14}C.

5.2. Carbon sources

Traditionally, DIC in groundwater has been deconvolved into distinct carbon pools using the methods developed by Chiodini et al. (2000, 2004), Crossey et al. (2009) and Karlstrom et al. (2013) (Fig. 3). However, this approach implicitly assumes that DIC is exclusively external or carbonate derived. While, the Chiodini et al. (2000, 2004) studies did in fact consider soil CO_2 derived DIC as a component of the external carbon, they did not measure ^{14}C as a means to estimate its overall contribution to the carbon pool. Instead, the Chiodini et al. (2000, 2004) approach assumed that soil CO_2 was added to the external carbon pool during infiltration of the water in the recharge areas. It was quantified by making assumptions about the original CO_2 atmospheric content of rain, plus biogenic soil C additions. Here, we take a slightly different approach and measure ^{14}C as a means to quantify the soil CO_2-derived DIC contribution. In contrast to the Chiodini et al. (2000, 2004) approach, we separate out surface derived soil-derived carbon (C_{soil}) and external carbon C_{ext} (slab and mantle) at each well location. We use radiocarbon data to estimate soil-derived carbon contributions (C_{soil}) to the aquifer. In our modified approach, we assume that 1) groundwater is relatively young, which is supported by measurable tritium in all samples, 2) no significant carbonate dissolution has occurred (silicate host rock should be carbonate free), 3) measured ^{14}C is a good approximation of initial ^{14}C (i.e., that no substantial decay has occurred) and 4) an initial atmosphere ^{14}C value of 125 pmc for samples with tritium >1 and an initial atmosphere ^{14}C value of 100 pmc for samples with tritium <1. We then classify "external CO_2" (C_{ext}) as the fraction of CO_2 that cannot be accounted for by soil CO_2 (C_{soil}) additions. Using $C/^3He$ values, C_{ext} is then further resolved into CO_2 components derived from the slab (C_{slab}) versus the mantle (C_{mantle}) (section 5.2.2). Finally, the slab component can be subdivided into subducted sediment ($C_{sediments}$) and limestone ($C_{limestone}$) contributions using a C-isotope mass balance approach (section 5.2.3).

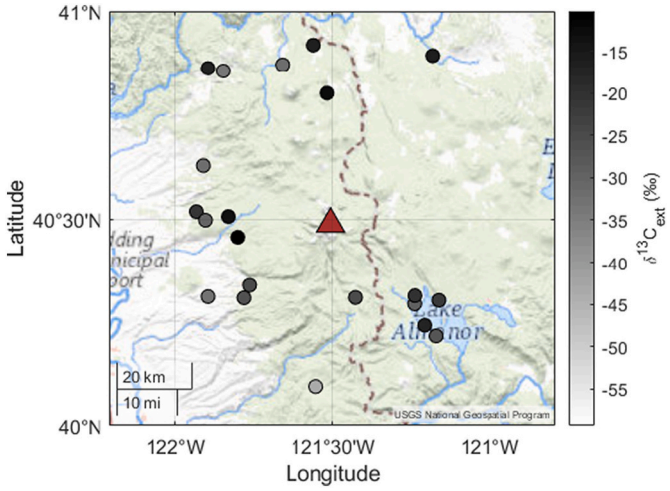

Fig. 8. Map showing the apparent external C isotope values as a function of latitude and longitude.

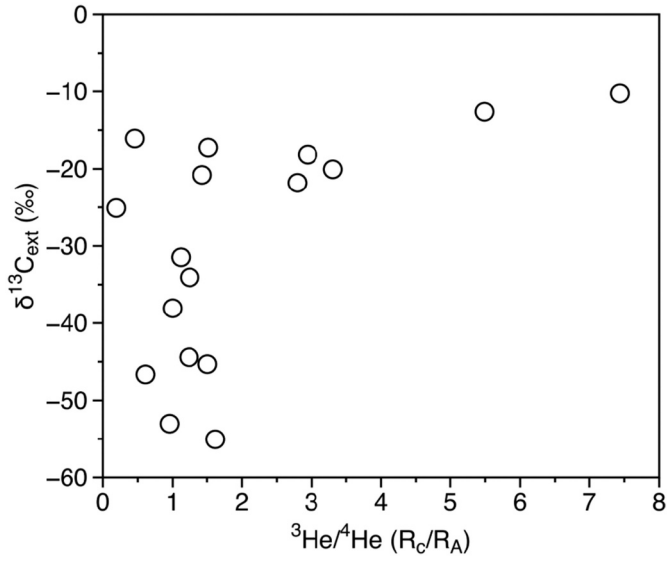

Fig. 9. The apparent external C isotope values as a function of air corrected He isotopes. The most mantle-like samples appear to have experienced the lowest degree of fractionation.

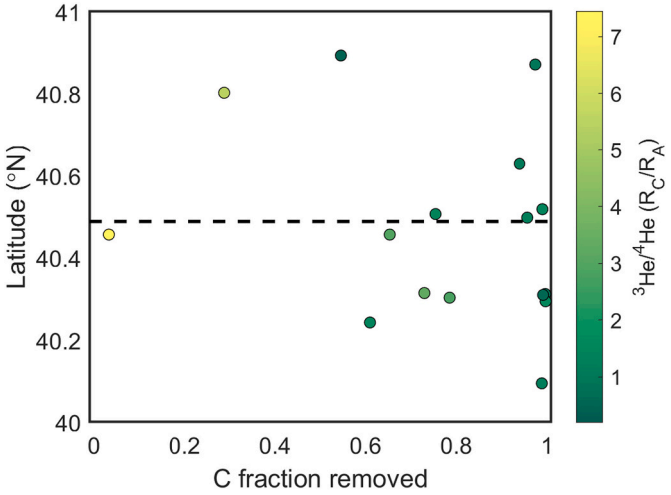

Fig. 10. Latitude vs C fraction (f) removed (Eq. 19). The samples with the lowest fraction removed from calcite precipitation are west of Lassen Peak (latitude shown with a black dashed line). This is also the locality that has the highest He isotope ratio (Camp Latieze).

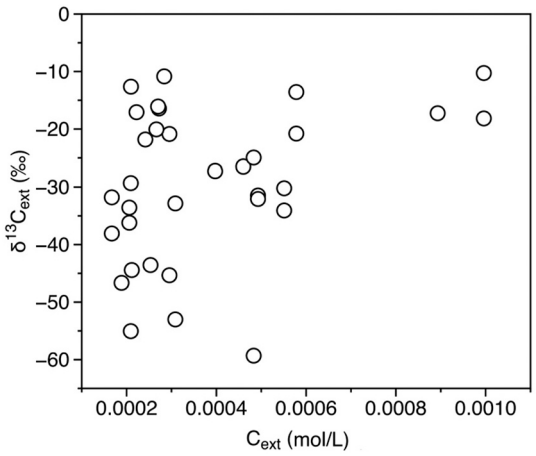

Fig. 11. The apparent external C isotope values as a function of C_{ext}. The samples with the lowest degree of fractionation (i.e., highest $\delta^{13}C_{ext}$) also have the highest Cext, suggesting that these samples are only moderately affected by secondary calcite precipitation processes and retain deep (mantle and slab) characteristics. These are also the samples with the highest He isotope ratios (Fig. 9).

5.2.1. External versus soil gas contributions

Here, radiocarbon (i.e., ^{14}C) data are used to estimate the overall antiquity of groundwater and the age of the carbon pool. We show that Lassen region groundwater samples experienced significant isotopic equilibration with soil gas CO_2, due to the biodegradation of C-rich surface material. Due to the fact that the soil gas reservoir is continuously being replenished by the decay of biogenic material, it can effectively be considered an infinite carbon reservoir, and as such, isotopic equilibrium should be achieved between soil CO_2 and the various components of DIC Seltzer et al., 2021. We note that negligible fractionation is often assumed between soil CO_2 and DIC, however this is likely oversimplified, because it is impossible to dissolve all carbon from an infinite reservoir and thus equilibrium fractionation likely occurs during dissolution (Vogel et al., 1970; Mook et al., 1974; Han and Plummer, 2013). Due to the fact that groundwater samples span a wide pH range from 5.8 to 8.5, the dominant species that compriseDIC are thus predicted to vary significantly. For example, in typical circumneutral groundwaters, almost all DIC is comprised of HCO_3^{2-}, however in more acidic groundwaters, CO_2 will also be an important component of DIC. Using this approach, we can (1) consider the equilibrium fractionation between soil CO_2 and DIC, and (2) tailor the equilibrium fractionation value to (ε) the known pH conditions at each well.

In this way, we add an important term to the approach of Chiodini et al., 2004 (Fig. 3). Radiocarbon (^{14}C) activities range from 47.4 to 108.6 pmc. The mean northern hemisphere atmospheric ^{14}C activity between 1955 and 2010 is assumed to be between 100 pmc (if $^3H < 1$) and 125 pmc (if $^3H > 1$) (Hua et al., 2013), thus allowing an estimation of surface carbon contributions to the groundwater system. Notably, this approach assumes negligible radiocarbon decay, due to the assumed short residence time of the groundwater, which is generally supported by tritium data. Further, we assume that the $\delta^{13}C$ of soil CO_2 ($\delta^{13}C_{soil}$) is ~ − 23‰ (Cerling et al., 1991; Clark and Fritz, 2013; Cartwright et al., 2020) and that the initial $\delta^{13}C$ of DIC is offset from soil CO_2 by the equilibrium fractionation (ε) at an assumed recharge temperature of 10 °C, that is sensitive to the speciation of DIC (Mook et al., 1974; Han and Plummer, 2013) in the groundwater system, which is ultimately governed by the pH. We estimate HCO_3^-/DIC and CO_2/DIC ratios using

CO2SYS software (Lewis and Wallace, 1998) to determine the equilibrium fractionation factor (ε) on a sample-by-sample basis, using Eq. 5, which ultimately allows for calculation of $\delta^{13}C_{soil,\ eq}$, using Eq. 6.

$$\varepsilon = (HCO_3^-/DIC) \times 9.60‰ + (CO_2/DIC) \times -1.13‰ \quad (5)$$

This approach assumes that if groundwaters are circumneutral (i.e., HCO_3^-/DIC is approaching 1 and CO_2/DIC is approaching 0), the fractionation factor (ε) is approaching +9.60‰ (i.e., the ^{13}C fractionation factor of gaseous CO_2 with respect to dissolved HCO_3^- at 10 °C; Han and Plummer, 2013), whereas if groundwater are more acidic (i.e., HCO_3^-/DIC is approaching 0 and CO_2/DIC is approaching 1), the fractionation factor approaches −1.13‰ (i.e., the ^{13}C fractionation factor of gaseous CO_2 with respect to dissolved CO_2 at 10 °C; Han and Plummer, 2013).

Once a ε value has been determined, the expected $\delta^{13}C$ of DIC in equilibrium with soil CO_2 ($\delta^{13}C_{soil,eq}$) can be calculated using Eq. 6:

$$\delta^{13}C_{soil,eq} = \delta^{13}C_{soil} + \varepsilon \quad (6)$$

Here we assume that Lassen region soil CO_2 ($\delta^{13}C_{soil}$) is ~ − 23‰ (e.g., Cartwright et al., 2020). Next, we estimate the fraction of DIC that is derived from soil CO_2 using measured ^{14}C of DIC ($^{14}C_{meas}$) from each individual well:

$$C_{soil} = \left(^{14}C_{meas}/^{14}C_{init}\right) \times DIC \quad (7)$$

In eq. 7, we assume that the initial ^{14}C ($^{14}C_{init}$) is either 100 pmC (if $^3H < 1$ TU) or 125 pmC (if $^3H > 1$ TU). We note that 7 of 37 samples (5 of 24 wells) have $^3H > 1$ Tritium Units (TU) and, given the hydrogeological setting and shallow well depths (all shallower than 141 m; average well depth is ~77 m), we assume that mean groundwater ages are all decadal to centennial. Thus, we neglect any decay of ^{14}C and treat it as a conservative tracer of soil-derived DIC, assuming no dissolution of carbonate minerals. Next, we estimate the DIC derived from an external source and its stable carbon isotopic composition by mass balance (eqs. 8 and 9):

$$C_{ext} = DIC - C_{soil} \quad (8)$$

$$\delta^{13}C_{ext} = \left(\delta^{13}C_{meas} - (C_{soil}/DIC) \times \delta^{13}C_{soil,eq}\right)/(C_{ext}/DIC) \quad (9)$$

We caution that this conceptual approach is highly sensitive to the assumed initial soil CO_2 endmember carbon isotopic composition, as well as the assumptions of short groundwater ages (i.e., negligible ^{14}C decay) and negligible carbonate dissolution. In turn, the estimate of C_{ext} is dependent on these same assumptions. We emphasize that several key samples (i.e., Camp Latieze) that are closest to Lassen Peak have low $^{14}C_{meas}$ but high tritium activities and high R_C/R_A, providing strong evidence that indeed young (decades-old) groundwater in the region with clear mantle helium input also seems to have low $^{14}C_{meas}$. These observations provide qualitative validation of these assumptions.

We assume that Ca + Mg contributions are from water-rock interaction with silicates, and that they do not contribute significantly to the carbon pool (i.e., as stated above, we assume there is no appreciable carbonate dissolution). Again, this approach differs from the approach adopted by Chiodini et al. (2004) and Crossey et al. (2009), which assumed that dissolution of carbonate minerals were significant, however the Lassen Peak region has a much different geological setting (i.e., silicate dominated). We thus do not apply a correction to data based on ion chemistry data and instead compute C_{ext} (in moles/L) for all Lassen Peak samples (Fig. 4) by simply subtracting C_{soil}. As a proportion of the total DIC, C_{ext} varies between 13% (Black Butte) and 62% (Camp Latieze) (Fig. 4), again assuming there is no significant carbonate dissolution contributing to the carbon pool.

5.2.2. Slab vs. mantle carbon – Using $C/^3He$

If we continue with this idealized modeling approach, based on the previous assumptions, we can attempt to break down C_{ext} into mantle and slab components. For example, external carbon (C_{ext}) can be further broken down into C_{mantle} and C_{slab} by applying mass balance constraints. First, we assume:

$$C_{ext} = C_{mantle} + C_{slab} \quad (10)$$

Then we estimate the excess ^3He in each sample by considering:

$$^3He_{excess} = {}^3He_{measured} - {}^3He_{ASW} - {}^3He_{EA} \quad (11)$$

The $^3He_{excess}$ is the measured ^3He corrected for ^3He additions from air equilibration and air bubble entrainment and represents the mantle derived helium component. $^3He_{excess}$ is used to calculate both the percent mantle helium in each sample and the mantle carbon (C_{mantle}) in each sample. To estimate the maximum amount of C_{mantle} (moles/L) in each sample, we combine $^3He_{excess}$ with the known $C/^3He$ of the mantle ($=2 \times 10^9$) using the Eq. 12 (Table 3):

$$C_{mantle} = \left(^3He_{excess}\right) \times \left(C/^3He_{mantle}\right) \quad (12)$$

The slab-derived C component is calculated from eqs. 8, 10, and 12.

C_{mantle} is small (average = ~4.2%) relative to C_{ext}, suggesting that the vast majority (>95%) of C_{ext} is non-mantle in origin (i.e., slab derived; Fig. 5 and Fig. 6). If we consider that ~19% of He (based on Eq. 4), on average, is derived from the mantle, then this observation suggests significant slab delivery of C into the magmatic system. Again, this estimate is heavily reliant on previous assumptions (i.e., that ^{14}C can be used as a conservative tracer to accurately estimate surface C and that the remaining external carbon pool is, in fact, from the slab and mantle). However, we note that there is not substantial ^3He in the downgoing slab (Bekaert et al., 2021), whereas the slab is considered C-rich (Varekamp et al., 1992). This results in orders of magnitude higher $C/^3He$ in subducting components vs. the mantle and the C signal in subduction zones to be dominated by subducting signatures. Crustal assimilation is ruled out on the basis of crust typically being isotopically high relative to the apparent external carbon isotopes observed here.

5.2.3. C_{ext} source variation

Following our idealized approach, we were able to estimate $\delta^{13}C_{ext}$ (Eq. 9; Table 2) by considering $\delta^{13}C_{soil,\ eq}$ on a well by well basis (Eq. 6), utilizing the estimate of the relative proportion of C_{soil} (estimated using ^{14}C) vs. C_{ext} (Eq. 7 and Eq. 8) for individual samples (Fig. 4; section 5.1.2). The apparent $\delta^{13}C$ of external DIC ranges between −10.3 and −59.3‰, with an average value of −29.3‰. We again caution that the resulting estimates of $\delta^{13}C_{ext}$ are highly sensitive to the estimated magnitude of C_{ext}, which itself is dependent on the various assumptions of short (<century) groundwater residence times, atmospheric values of soil CO_2, ^{14}C activity, and negligible carbonate dissolution.

Next, we attempt to determine the source of the apparently very light C isotopes in the samples. We know that a very small fraction (~4.2%) of the external C (and thus the $\delta^{13}C_{ext\text{-}app}$) comes from the mantle ($F_{mantle} = C_{mantle}/C_{ext}$). Here, we use Eq. 13 to estimate $\delta^{13}C_{slab}$:

$$\delta^{13}C_{slab} = \delta^{13}C_{ext} - \left(\delta^{13}C_{mantle}\ F_{mantle}\right)/(1 - F_{mantle}) \quad (13)$$

We can now take the solution from Eq. 13 and plug it into Eq. 14 and solve for the fraction of sediment and limestone in the samples, by assuming that $F_{limestone} = 1 - F_{sediment}$ and assuming endmember values of $\delta^{13}C_{sediment} = -40‰$ and $\delta^{13}C_{limestone} = 0‰$.

$$F_{sediment} = \left(\delta^{13}C_{slab} - \delta^{13}C_{limestone}\right)/\left(\delta^{13}C_{sediment} - \delta^{13}C_{limestone}\right) \quad (14)$$

This approach assumes that the fraction of C_{ext} is a simple two-component mixture, calculated assuming $\delta^{13}C_{slab} = -40‰$ and $\delta^{13}C_{mantle} = -5‰$, and considering that $C_{slab} + C_{mantle} = C_{ext}$. With knowledge of the limited input of C_{mantle} to the overall mass balance, C_{slab} signatures can be explained by an admixture of $C_{sediment}$ and $C_{limestone}$, both of which are subduction-derived. In this way, the composition of the slab-derived fluids can be estimated. Not surprisingly, due to the overwhelmingly negative C_{ext} isotope values observed in Lassen samples (−29.3‰ on average), a dominantly $C_{sediment}$ subduction

package is required to explain the data, again assuming $\delta^{13}C_{sediment} = -40‰$, $\delta^{13}C_{limestone} = -0‰$ and $\delta^{13}C_{mantle} = -5‰$. Even with an extreme sediment endmember of −40‰ however, not all data can be explained due to mixing (i.e., those with $\delta^{13}C_{ext} < -40‰$).

This approach requires (1) an extremely light and improbable $\delta^{13}C_{sediment}$ of −40‰ or lighter (~ −60‰), as well as (2) large variations in slab-derived sediment and limestone contributions, which also seem unlikely on such a small spatial-scale. Even with these assumptions, we still cannot explain all observed data. Thus, we conclude here that the Sano and Marty (1995) mixing approach is not viable and we present an alternative, process-driven model in the following section.

5.3. Fractionation model

In the above section we showed that in any mixing scenario, C_{ext} must be dominated by unrealistically light $\delta^{13}C_{slab}$ additions. An alternative interpretation of the isotopically light C isotope values is that they are derived from fractionation processes during fluid transit to the surface. In this alternative model, $\delta^{13}C_{ext}$ variations are explained entirely by calcite precipitation, a process that has previously been proposed in several other subduction zones (i.e., Ray et al., 2009; Tardani et al., 2016; Barry et al., 2019a, 2019b; Barry et al., 2020). This model therefore explains all $\delta^{13}C_{ext}$ variability using a non-mixing scenario, where the isotopically light signatures in $\delta^{13}C_{ext}$ result from calcite precipitation-induced fractionation. In this way, we can predict what the initial C isotope values must have been (i.e., $\delta^{13}C_{ext\text{-}init}$) prior to any fractionation.

Here, we start with the observation that apparent $\delta^{13}C_{ext}$ varies between −10.3‰ and − 59.3‰ in Lassen samples (Table 3), following correction for soil CO_2. We note that if there was no isotopic fractionation, we would predict a single reproducible value for $\delta^{13}C_{ext}$ to describe all data in the system (i.e., one pure, unfractionated source). This wide range is incompatible with a single, unfractionated external source of carbon. Variable fractionation associated with spatially heterogeneous calcite precipitation could however lead to a wide range of $\delta^{13}C_{ext}$ across samples. We assume that $\delta^{13}C_{ext}$ must have initially been isotopically heavier, as source values approaching −60‰ do not have a viable source (i.e., a sediment endmember is likely much closer to −20‰ and limestone is approximately 0‰). Isotopic fractionation due to calcite precipitation varies as a function of temperature, with an inflection point ~193 °C (Ohmoto and Rye, 1979). Thus, we can reasonably assume that the fractionation of $\delta^{13}C_{external}$ must have occurred below this 193 °C threshold. To explain all data at a single temperature, the extent of fractionation (Fig. 7) between initial and apparent $\delta^{13}C_{ext}$ values (i.e., $\delta^{13}C_{ext\text{-}init}$ - $\delta^{13}C_{ext}$) must be large ~49‰ (i.e., −10.3‰ – -59.3‰).

Hence, we take the empirically derived fractionation between DIC and calcite from Ohmoto and Rye, 1979:

$$1000 \times \ln\alpha DIC - calcite = -8.914 \times 10^{8} T^{-3} + 8.557 \times 10^{6} T^{-2} - 18.11 \times 10^{3} T^{-1} + 8.27 \quad (15)$$

and rearrange eq. 17 to solve for alpha α:

$$\alpha = \mathrm{Exp}\left(\left(= -8.914 \times 10^{8}/T^{3} + 8.557 \times 10^{6}/T^{2} - 18.11 \times 10^{3}/T + 8.27\right)/1000\right) \quad (16)$$

where T is the temperature in Kelvin.

If we assume a temperature of 50 °C (= 323.15 K) and solve for α, we can then rearrange Eq. 17 (i.e., the Rayleigh distillation equation; Holloway and Blank, 2018) to solve for f (Eq. 18) in each sample, where f is defined as the fraction of C removed from DIC due to calcite precipitation.

We assume a common $\delta^{13}C_{ext\text{-}init}$ (= − 10‰) for all samples and assume that all isotopic variability observed is due to calcite precipitation. Hence, apparent and initial carbon isotopes can be related using the following equation:

$$\delta^{13}C_{ext} = \left(\delta^{13}C_{ext-init} + 1000\right)\left(f^{\alpha-1}\right) - 1000 \quad (17)$$

where $\delta^{13}C_{ext}$ is the apparent carbon isotope composition of DIC at a given temperature, $\delta^{13}C_{ext\text{-}init}$ is the initial isotope composition of the DIC (assumed to be −10‰,), and α is the fractionation factor between DIC and calcite at a given temperature. We can now rearrange these expressions to solve for f at a given temperature:

$$f = 1 - \left[\left(\mathrm{Exp}\left(\mathrm{Ln}\left(\left(\delta^{13}C_{ext} + 1000\right)/\left(\delta^{13}C_{ext-init} + 1000\right)\right)/(\alpha - 1)\right)\right)\right] \quad (18)$$

Neither the assumed temperature (=50 °C) nor the $\delta^{13}C_{ext\text{-}init}$ (= −10‰) are unique "input variables" (Fig. 7); rather, they are only used to 1) illustrate the viability of this conceptual approach, and 2) explore the parameter space that can explain the observations. Here, we assume that there is a common source of external C ($\delta^{13}C_{ext\text{-}init}$) with a $\delta^{13}C$ value of −10‰ that was subsequently fractionated to variable extents as calcite precipitated. This scenario appears more likely than wildly different slab contributions from sediments vs. limestones between wells located just a few kilometers apart (i.e., the source variation and mixing model presented above). In the past, researchers have attributed such large C isotope variations to admixtures of different source contributions when investigating high temperature volcanic crater gas emissions with significant mantle contributions. Here, however, we are investigating groundwaters with relatively small mantle contributions, so such a mixing approach may not be appropriate. Using C/^{3}He, we showed that mantle C contributions must be <5%, thus making our alternative model more palatable than a simple mixing scenario.

We show in Fig. 8 that the extent of C isotope fractionation is somewhat regionally correlated, with the isotopically heaviest C isotope values occurring directly to the west of Lassen Peak (i.e., the Camp Latieze sample, which also has the highest R_C/R_A value; Fig. 9). In the calcite fractionation model, these are the samples that require the least C removal, suggesting they are the most pristine samples that retain deep C and He isotope characteristics. In fact, the highest He isotope value observed occurs in Camp Latieze, which also has the lowest predicted fraction of C removed (Fig. 9). Notably, this sample is at the same latitude as Lassen Peak (black dashed line, Fig. 10), however latitudinal correlations are not clear from a regional perspective. There is a correlation between radial distance to Lassen Peak with He isotopes (Fig. S2), but no clear correlation between $\delta^{13}C_{ext}$ (Fig. S3) or the fraction (f) of carbon removed due to calcite precipitation (Fig. S4). These trends suggest a relatively direct conduit for mantle-derived volatiles, which results in higher He isotopes and less modified C systematics near Lassen Peak (Fig. 10, 11). Samples to the north and south typically show >60% C removal due to calcite precipitation (Fig. 7) and generally more radiogenic He isotope values, perhaps due to the increased interaction with the crust during longer volatile transit to the surface.

5.4. Carbon flux calculations

With estimates of external carbon contributions C_{ext} to Lassen water samples, we can now estimate the maximum flux of external C transported by groundwaters out of the Lassen region. Carbon flux estimates represent maximum values due to the inherent assumptions used to estimate C_{ext}, most importantly the assumptions concerning ^{14}C. That is, if ^{14}C of soil CO_2 is in fact sub-atmospheric (Cartwright et al., 2020), if the groundwater is older than we suspect (such that ^{14}C has decayed), or if there has been appreciable carbonate dissolution, our estimates of C_{ext} would be an overestimation. We combine C_{ext} values with estimates of cold spring flow rates (Rose and Davisson, 1996; Davisson and Rose, 1997). We know that external carbon (C_{ext}) is composed of C_{slab} and C_{mantle} and thus we can estimate mantle- vs. slab-derived C fluxes. Here, it is critical to consider nomenclature. Rose and Davisson, 1996 previously estimated a "magmatic DIC flux" of 1.1 × 10^7 kg/yr, which is

comparable to what we call "external DIC flux". These authors used ^{14}C to estimate the "magmatic" fraction of DIC from the Lassen region to be 25–60%, and then combined this with measured DIC and flowrates from nearby springs to make a first order estimate of the deep (non-atmospheric) C flux to the surface (i.e., what they called magmatic C flux). If we adopt a similar method, using identical fluid discharge estimates (= 1.5×10^4 L/s; Rose and Davisson, 1996) and the average C_{ext} value (= 0.386 mmol/L) from our study, we calculate a slightly lower flux of "external C" (2.2×10^6 kg/yr). However, the He—C mass balance approach that we adopt (Section 5.2.2) indicates that only ~4.2% of the C_{ext} is mantle-derived on average. This calculation therefore implies that the actual mantle flux is actually much lower (5.3×10^4 kg/yr) than previously considered, and that the bulk of the C (>95%) emitted at the surface is slab-derived. This is an important nuance between the two approaches: while the approach used by Rose and Davisson can identify external C fluxes (referred to "magmatic" fluxes), the clear advantage of the He—C approach is that it provides additional insight into the source (s) of that external C (i.e., slab vs. mantle). We suggest that future studies adopt a coupled noble gas-^{13}C-^{14}C approach, which will provide robust constraints on the C sources feeding volcanic aquifer systems.

Davisson and Rose (1997) later updated fluid discharge rates for the region (7.8×10^4 L/s (Davisson and Rose, 1997) vs. 1.5×10^4 L/s (Rose and Davisson, 1996)). Thus passive dissolved C fluxes could be greater by a factor of five for the entire Lassen region. If we adopt the higher discharge rate, we calculate an external flux of 1.1 x 10^7kg/yr. However, we note that discharge rate estimates are poorly constrained and temporally variable (Rose et al., 1996). Spring flow rates proximal to Lassen Peak respond to transient changes in permeability associated with earthquakes (Ingebritsen et al., 2015). Changes in spring flow rates on short timescales means that C flux from the Lassen region could vary seasonally, annually and inter-annually.

In summary, we estimate an external C flux of 2.2×10^6 kg/yr at Lassen, which is lower than previous estimates by Rose and Davisson, 1996. To compare our DIC flux estimates with previously estimated geothermal C degassing fluxes from the Lassen Peak area, we again adopt the approach of Rose and Davisson (1996) and assume that ~79% of deeply-derived DIC is in the form of HCO_3^-, which is equivalent to 1.3×10^6 kg/yr of magmatic CO_2 gas. Published gas chemistry data (Muffler et al. (1982); Janik and Bergfeld (2010)) and mass flux estimates (Sorey and Colvard (1994)) for the Lassen Peak geothermal system can be combined to calculate a total geothermal CO_2 degassing rate. This estimate assumes that the vapor-dominated geothermal reservoir at Lassen Peak has 1) a H_2O/gas ratio of ~85, and 2) a gas phase that contains 92.7 mol% CO_2 (Rose and Davisson, 1996). The bulk CO_2 concentration in the steam discharge is therefore ~2.7% by weight. The estimated steam discharge rate from the geothermal system is 41 kg/s, which implies a total CO_2 gas geothermal degassing rate of $\sim 3.5 \times 10^7$ kg/yr (Rose and Davisson (1996)). This estimate agrees well with CO_2 flux estimates of $\sim 0.7–4.0 \times 10^7$ kg/yr determined from subsequent airborne surveys which employed a nondispersive infrared CO_2 analyzer and flow control unit to measure CO_2 concentrations (Gerlach et al., 2008). Thus, the total external flux that we calculate in this study would correspond to ~4–18% of the geothermal CO_2 degassing rate, whereas the mantle carbon flux would only be equivalent to ~0.2–0.8% of the estimated geothermal CO_2 gas flux at Lassen, depending on which discharge rate we assume (Rose and Davisson (1996); Davisson and Rose (1997)), respectively. Assuming the lower discharge rate of Rose and Davisson (1996), the entire external C flux of 2.2×10^6 kg/yr at Lassen, is more than an order of magnitude smaller than soil CO_2 flux estimates ($7.3–11 \times 10^7$ kg/yr) for nearby volcanoes (Sorey et al., 1998; Gerlach et al., 1999), suggesting that passive dissolved carbon fluxes are relatively small compared with diffuse soil and geothermal CO_2 degassing fluxes. This is an important consideration for the global carbon budget, as passive carbon fluxes represent an important, yet poorly constrained portion of the geogenic carbon flux. Future studies should better characterize passive carbon fluxes from arcs worldwide as well as prominent non-arc volcanic systems e.g., Yellowstone and the Rio Grande Rift (Blomgren et al., 2019).

6. Summary

Understanding carbon isotopic signatures and the processes that affect them are critical to make accurate volcanic flux estimates and identify the origin of carbon. In this contribution, we investigate sources and sinks of C dissolved in groundwaters around Lassen Peak in California. Radiocarbon data are used to distinguish soil-derived carbon from external carbon; slab vs. mantle contributions are estimated using C/^{3}He mass balance constraints. Carbon isotopes in fluids are then used to explore two independent models; the first is a mixing model (after Sano and Marty, 1995) and the second is a conceptual calcite precipitation fractionation model. We strongly favor the second model because it does not require an implausibly light source $\delta^{13}C$ (i.e., extremely light organic sediment contributions to the slab) or large variations in the slab contributions at the local scale. We caution that all models are highly dependent on the assumptions made in regards to the soil CO_2 correction. This model nonetheless suggests that the effect of calcite precipitation on C isotopes in volcanic systems may be under-appreciated. Finally, we estimate the maximum external (slab and mantle) C flux to be $\sim 2.2 \times 10^6$ kg/yr, lower than previous C flux estimates (Rose and Davisson (1996)). This represents ~4–18% of the geothermal CO_2 flux (estimated to be 3.5×10^7 kg/yr), which is more than an order of magnitude smaller than soil gas CO_2 flux estimates ($7.3–11 \times 10^7$ kg/yr) for nearby volcanoes (Sorey et al., 1998; Gerlach et al., 1999). These data indicate significant transport and release of slab C in the greater vicinity (~60 km) of the Lassen volcanic edifice, yet a relatively small mantle contribution. We emphasize that future studies should measure all noble gases (to ensure robust excess air corrections), ^{14}C (to estimate soil CO_2 contributions) and ^3H (to justify the use of ^{14}C as a conservative tracer; i.e., no significant decay). Only with these data in hand can deep carbon fluxes be accurately estimated and compared with geothermal CO_2 gas and soil gas fluxes, all of which are needed to obtain an accurate estimate of a given volcano's total deep C footprint.

Declaration of Competing Interest

The authors declare that they have no known competing financial interests or personal relationships that could have appeared to influence the work reported in this paper.

Acknowledgments

This work is dedicated to the late David Hilton, who provided friendship, guidance, and opportunity to several of the co-authors, especially to PHB. This work stems in part from BPF's master's thesis. We thank Pat Castillo and James Day for serving on BPF's committee and comments on his thesis. We acknowledge Bruce Deck for training and guidance on the IRMS. Funding was provided by the Deep Carbon Observatory Reservoirs and Fluxes Directorate. PHB acknowledges NSF awards 1923915 and 2015789, which supported him during the writeup of this project. Any use of trade, firm, or product names is for descriptive purposes only and does not imply endorsement by the U.S. Government.

Appendix A. Supplementary data

Supplementary data to this article can be found online at https://doi.org/10.1016/j.chemgeo.2021.120535.

References

Aeschbach-Hertig, W., Solomon, D.K., 2013. Noble gas thermometry in groundwater hydrology. In: The Noble Gases as Geochemical Tracers, pp. 81–122.

Aeschbach-Hertig, W., Peeters, F., Beyerle, U., Kipfer, R., 2000. Palaeotemperature reconstruction from noble gases in ground water taking into account equilibration with entrapped air. Nature 405 (6790), 1040–1044.
Aiuppa, A., Fischer, T.P., Plank, T., Bani, P., 2019. CO 2 flux emissions from the Earth's most actively degassing volcanoes, 2005–2015. Sci. Rep. 9 (1), 1–17.
Allard, P., Jean-Baptiste, P., D'Alessandro, W., Parello, F., Parisi, B., Flehoc, C., 1997. Mantle-derived helium and carbon in groundwaters and gases of Mount Etna, Italy. Earth Planet. Sci. Lett. 148 (3–4), 501–516.
Anderson, C.A., 1940. Hat Creek lava flow. Am. J. Sci. 238 (7), 477–492.
Barry, P.H., Hilton, D.R., Fischer, T.P., De Moor, J.M., Mangasini, F., Ramirez, C., 2013. Helium and carbon isotope systematics of cold "mazuku" CO2 vents and hydrothermal gases and fluids from Rungwe Volcanic Province, southern Tanzania. Chem. Geol. 339, 141–156.
Barry, P.H., Hilton, D.R., Füri, E., Halldórsson, S.A., Grönvold, K., 2014. Carbon isotope and abundance systematics of Icelandic geothermal gases, fluids and subglacial basalts with implications for mantle plume-related CO2 fluxes. Geochim. Cosmochim. Acta 134, 74–99.
Barry, P.H., de Moor, J.M., Giovannelli, D., Schrenk, M.O., Hummer, D.R., Lopez, T., Pratt, C.A., Alpízar Segura, Y., Battaglia, A., Beaudry, P., Bini, G., Cascante, M., D'errico, G., Di Carlo, M., Fattorini, D., Fullerton, K., Gazel, E., González, G., Halldórsson, S.A., Iacovino, K., Kulongoski, J.T., Manini, E., Martínez, M., Miller, H., Nakagawa, M., Ono, S., Patwardhan, S., Ramírez, C.J., Regoli, F., Smedile, F., Turner, S., Vetriani, C., Yücel, M., Ballentine, C.J., Fischer, T.P., Hilton, D.R., Lloyd, K.G., 2019a. Forearc carbon sink reduces long-term volatile recycling into the mantle. Nature 568 (7753), 487–492.
Barry, P.H., Nakagawa, M., Giovannelli, D., de Momor, J.M., Schrenk, M., Seltzer, A.M., Manini, E., Fattorini, D., di Carlo, M., Regoli, F., Fullerton, and K., Lloyd, K.G., 2019b. Helium, inorganic and organic carbon isotopes of fluids and gases across the Costa Rica convergent margin. Sci. Data 6 (1), 1–8.
Barry, P.H., Negrete-Aranda, R., Spelz, R.M., Seltzer, A.M., Bekaert, D.V., Virrueta, C., Kulongoski, J.T., 2020. Volatile sources, sinks and pathways: A helium-carbon isotope study of Baja California fluids and gases. Chem. Geol. 550, 119722.
Bekaert, D.V., Turner, S.J., Broadley, M.W., Barnes, J.D., Halldórsson, S.A., Labidi, J., Wade, J., Walowski, K.J., Barry, P.H., 2021. Subduction-Driven Volatile Recycling: A Global Mass Balance. Annu. Rev. Earth Planet. Sci. 49.
Bergfeld, D., Evans, W.C., Howle, J.F., Farrar, C.D., 2006. Carbon dioxide emissions from vegetation-kill zones around the resurgent dome of Long Valley caldera, eastern California, USA. J. Volcanol. Geotherm. Res. 152 (1–2), 140–156.
Bergfeld, D., Evans, W.C., Spicer, K.R., Hunt, A.G., Kelly, P.J., 2017. Evidence for degassing of fresh magma during the 2004–2008 eruption of Mount St. Helens: Subtle signals from the hydrothermal system. J. Volcanol. Geotherm. Res. 343, 109–121.
Blomgren, V.J., Crossey, L.J., Karlstrom, K.E., Fischer, T.P., Darrah, T.H., 2019. Hot spring hydrochemistry of the Rio Grande rift in northern New Mexico reveals a distal geochemical connection between Valles Caldera and Ojo Caliente. J. Volcanol. Geotherm. Res. 387, 106663.
Cartwright, I., Currell, M.J., Cendón, D.I., Meredith, K.T., 2020. A review of the use of radiocarbon to estimate groundwater residence times in semi-arid and arid areas. J. Hydrol. 580, 124247.
Cerling, T.E., Solomon, D.K., Quade, J.A.Y., Bowman, J.R., 1991. On the isotopic composition of carbon in soil carbon dioxide. Geochim. Cosmochim. Acta 55 (11), 3403–3405.
Chiodini, G., Frondini, F., Kerrick, D.M., Rogie, J., Parello, F., Peruzzi, L., Zanzari, A.R., 1999. Quantification of deep CO2 fluxes from Central Italy. Examples of carbon balance for regional aquifers and of soil diffuse degassing. Chem. Geol. 159 (1–4), 205–222.
Chiodini, G., Frondini, F., Cardellini, C., Parello, F., Peruzzi, L., 2000. Rate of diffuse carbon dioxide Earth degassing estimated from carbon balance of regional aquifers: the case of central Apennine, Italy. J. Geophys. Res. Solid Earth 105 (B4), 8423–8434.
Chiodini, G., Cardellini, C., Amato, A., Boschi, E., Caliro, S., Frondini, F., Ventura, G., 2004. Carbon dioxide Earth degassing and seismogenesis in central and southern Italy. Geophys. Res. Lett. 31 (7).
Clark, I.D., Fritz, P., 2013. Environmental Isotopes in Hydrogeology. CRC press.
Clynne, M.A., 1990. Stratigraphic, lithologic, and major element geochemical constraints on magmatic evolution at Lassen Volcanic Center, California. J. Geophys. Res. Solid Earth 95 (B12), 19651–19669.
Cockerham, R.S., 1984. Evidence for a 180-km-long subducted slab beneath northern California. Bull. Seismol. Soc. Am. 74 (2), 569–576.
Craig, H., Lupton, J.E., Welhan, J.A., Poreda, R., 1978. Helium isotope ratios in Yellowstone and Lassen Park volcanic gases. Geophys. Res. Lett. 5 (11), 897–900.
Crossey, L.J., Karlstrom, K.E., Springer, A.E., Newell, D., Hilton, D.R., Fischer, T., 2009. Degassing of mantle-derived CO2 and he from springs in the southern Colorado Plateau region—Neotectonic connections and implications for groundwater systems. Geol. Soc. Am. Bull. 121 (7–8), 1034–1053.
Crossey, L.J., Karlstrom, K.E., Schmandt, B., Crow, R.R., Colman, D.R., Cron, B., Takacs-Vesbach, C.D., Dahm, C.N., Northup, D.E., Hilton, D.R., Ricketts, J.W., 2016. Continental smokers couple mantle degassing and distinctive microbiology within continents. Earth Planet. Sci. Lett. 435, 22–30.
Davisson, M.L., Rose, T.P., 1997. Comparative isotope hydrology study of groundwater sources and transport in the three cascade volcanoes of northern California (no. UCRL-ID-128423). Lawrence Livermore National Lab.(LLNL), Livermore, CA (United States).
Dickson, A.G., Afghan, J.D., Anderson, G.C., 2003. Reference materials for oceanic CO2 analysis: a method for the certification of total alkalinity. Mar. Chem. 80 (2–3), 185–197.
EPA, Environmental Monitoring Systems Laboratory (Cincinnati and Ohio), 1993. Methods for the Determination of Inorganic Substances in Environmental Samples, Vol. 600. United States Environmental Protection Agency, Office of Research and Development.
Evans, W.C., Sorey, M.L., Cook, A.C., Kennedy, B.M., Shuster, D.L., Colvard, E.M., White, L.D., Huebner, M.A., 2002. Tracing and quantifying magmatic carbon discharge in cold groundwaters: lessons learned from Mammoth Mountain, USA. J. Volcanol. Geotherm. Res. 114 (3–4), 291–312.
Fischer, T.P., Arellano, S., Carn, S., Aiuppa, A., Galle, B., Allard, P., Lopez, T., Shinohara, H., Kelly, P., Werner, C., Cardellini, C., 2019. The emissions of CO 2 and other volatiles from the world's subaerial volcanoes. Sci. Rep. 9 (1), 1–11.
Fishman, M.J., Friedman, L.C., 1989. Methods for Determination of Inorganic Substances in Water and Fluvial Sediments. US Department of the Interior, Geological Survey.
Garbarino, J.R., Struzeski, T.M., 1998. Methods of Analysis by the US Geological Survey National Water Quality Laboratory: Determination of elements in Whole-water Digests using Inductively coupled Plasma-optical Emission Spectrometry and Inductively coupled Plasma-mass Spectrometry (p. 101). US Department of the Interior, US Geological Survey.
Garbarino, J.R., Kanagy, L.K., Cree, M.E., 2006. Determination of Elements in Natural-Water, Biota, Sediment, and Soil Samples using Collision/Reaction Cell Inductively Coupled Plasma-Mass Spectrometry. US Department of the Interior, US Geological Survey, p. 88.
Gerlach, T.M., 1991. Present-day CO2 emissions from volcanos. EOS Trans. Am. Geophys. Union 72 (23), 249–255.
Gerlach, T.M., Doukas, M.P., McGee, K.A., Kessler, R., 1999. Airborne detection of diffuse carbon dioxide emissions at Mammoth Mountain, California. Geophys. Res. Lett. 26 (24), 3661–3664.
Gerlach, T.M., McGee, K.A., Doukas, M.P., 2008. Emission rates of CO2, SO2, and H2S, scrubbing, and preeruption excess volatiles at Mount St. Helens, 2004-2005 no. 1750-26. US Geological Survey, pp. 543–571.
Graham, D.W., 2002. Noble gas isotope geochemistry of mid-ocean ridge and ocean island basalts: Characterization of mantle source reservoirs. Rev. Mineral. Geochem. 47 (1), 247–317.
Gran, G., 1952. Determination of the equivalence point in potentiometric titrations. Part II. Analyst 77 (920), 661–671.
Guffanti, M., Weaver, C.S., 1988. Distribution of late Cenozoic volcanic vents in the Cascade Range: Volcanic arc segmentation and regional tectonic considerations. J. Geophys. Res. Solid Earth 93 (B6), 6513–6529.
Halldórsson, S.A., Scarsi, P., Abebe, T., Evans, T., Kulongoski, J.T., Castillo, P.R., Barry, P.H., Hilton, D.R., 2021. He-CO2-N2 Isotope and Relative Abundance Characterization of Geothermal Fluids from the Ethiopian Rift, Proceedings World Geothermal Congress, Reykjavik, Iceland, 2021 (Extended abstract).
Han, L.F., Plummer, L.N., 2013. Revision of Fontes & Garnier's model for the initial 14C content of dissolved inorganic carbon used in groundwater dating. Chem. Geol. 351, 105–114.
Heaton, T.H.E., Vogel, J.C., 1981. "Excess air" in groundwater. J. Hydrol. 50, 201–216.
Hilton, D.R., 1996. The helium and carbon isotope systematics of a continental geothermal system: results from monitoring studies at Long Valley caldera (California, USA). Chem. Geol. 127 (4), 269–295.
Hilton, D.R., Fischer, T.P., Marty, B., 2002. Noble gases and volatile recycling at subduction zones. Rev. Mineral. Geochem. 47 (1), 319–370.
Holloway, J.R., Blank, J.G., 2018. Application of experimental results to COH species in natural melts. Rev. Mineral. 30, 187–230.
Hua, Q., Barbetti, M., Rakowski, A.Z., 2013. Atmospheric radiocarbon for the period 1950–2010. Radiocarbon 55 (4), 2059–2072.
Ingebritsen, S.E., Evans, W.C., 2019. Potential for increased hydrothermal arsenic flux during volcanic unrest: Implications for California water supply. Appl. Geochem. 108, 104384.
Ingebritsen, S.E., Shelly, D.R., Hsieh, P.A., Clor, L.E., Seward, P.H., Evans, W.C., 2015. Hydrothermal response to a volcano-tectonic earthquake swarm, Lassen, California. Geophys. Res. Lett. 42 (21), 9223–9230.
Ingebritsen, S.E., Bergfeld, D., Clor, L.E., Evans, W.C., 2016. The Lassen hydrothermal system. Am. Mineral. 101 (2), 343–354.
James, E.R., Manga, M., Rose, T.P., 1999. CO2 degassing in the Oregon Cascades. Geology 27 (9), 823–826.
James, E.R., Manga, M., Rose, T.P., Hudson, G.B., 2000. The use of temperature and the isotopes of O, H, C, and noble gases to determine the pattern and spatial extent of groundwater flow. J. Hydrol. 237 (1–2), 100–112.
Janik, C.J., Bergfeld, D., 2010. Analyses of Gas, Steam and Water Samples Collected in and Around Lassen Volcanic National Park, California, pp. 1975–2002.
Janik, C.J., McLaren, M.K., 2010. Seismicity and fluid geochemistry at Lassen Volcanic National Park, California: evidence for two circulation cells in the hydrothermal system. J. Volcanol. Geotherm. Res. 189 (3–4), 257–277.
Karlstrom, K.E., Crossey, L.J., Hilton, D.R., Barry, P.H., 2013. Mantle 3He and CO2 degassing in carbonic and geothermal springs of Colorado and implications for neotectonics of the Rocky Mountains. Geology 41 (4), 495–498.
Kennedy, B.M., Kharaka, Y.K., Evans, W.C., Ellwood, A., DePaolo, D.J., Thordsen, J., Ambats, G., Mariner, R.H., 1997. Mantle fluids in the San Andreas fault system, California. Science 278 (5341), 1278–1281.
Kulongoski, J.T., Hilton, D.R., 2002. A quadrupole-based mass spectrometric system for the determination of noble gas abundances in fluids. Geochem. Geophys. Geosyst. 3 (6), 1–10.
Kulongoski, J.T., Hilton, D.R., 2012. Applications of groundwater helium. In: Handbook of Environmental Isotope Geochemistry, pp. 285–304.

Kulongoski, J.T., Hilton, D.R., Izbicki, J.A., 2003. Helium isotope studies in the Mojave Desert, California: implications for groundwater chronology and regional seismicity. Chem. Geol. 202 (1–2), 95–113.
Kulongoski, J.T., Hilton, D.R., Izbicki, J.A., 2005. Source and movement of helium in the eastern Morongo groundwater Basin: the influence of regional tectonics on crustal and mantle helium fluxes. Geochim. Cosmochim. Acta 69 (15), 3857–3872.
Kulongoski, J.T., Hilton, D.R., Barry, P.H., Esser, B.K., Hillegonds, D., Belitz, K., 2013. Volatile fluxes through the big Bend section of the San Andreas Fault, California: Helium and carbon-dioxide systematics. Chem. Geol. 339, 92–102.
Lee, H., Muirhead, J.D., Fischer, T.P., Ebinger, C.J., Kattenhorn, S.A., Sharp, Z.D., Kianji, G., 2016. Massive and prolonged deep carbon emissions associated with continental rifting. Nat. Geosci. 9 (2), 145–149.
Lewis, E.R., Wallace, D.W.R., 1998. *Program developed for CO2 system calculations* (no. cdiac: CDIAC-105). In: Environmental System Science Data Infrastructure for a Virtual Ecosystem.
Lupton, J.E., 1983. Terrestrial inert gases: Isotope tracer studies and clues to primordial components in the mantle. Annu. Rev. Earth Planet. Sci. 11 (1), 371–414.
Marty, B., Le Cloarec, M.F., 1992. Helium-3 and CO2 fluxes from subaerial volcanoes estimated from polonium-210 emissions. J. Volcanol. Geotherm. Res. 53 (1–4), 67–72.
Marty, B., Jambon, A., Sano, Y., 1989. Helium isotopes and CO2 in volcanic gases of Japan. Chem. Geol. 76 (1–2), 25–40.
McNichol, A.P., Jones, G.A., Hutton, D.L., Gagnon, A.R., Key, R., 1994. The rapid preparation of seawater ΣCO2 for radiocarbon analysis at the National Ocean Sciences AMS Facility. Radiocarbon 36 (2), 237–246.
Mook, W.G., Bommerson, J.C., Staverman, W.H., 1974. Carbon isotope fractionation between dissolved bicarbonate and gaseous carbon dioxide. Earth Planet. Sci. Lett. 22 (2), 169–176.
Morrison, P., Pine, J., 1955. Radiogenic origin of the helium isotopes in rock. Ann. N. Y. Acad. Sci. 62 (3), 71–92.
Muffler, L.J.P., Nehring, N.L., Truesdell, A.H., Janik, C.J., Clynne, M.A., Thompson, J.M., 1982. The Lassen Geothermal System. Proceedings of the Pacific Geothermal Conference 1982. *Part*, *2*, pp. 349–356.
Ohmoto, H., Rye, R.O., 1979. In: Barnes, H.L. (Ed.), Geochemistry of Hydrothermal Ore Deposits, pp. 509–567.
O'nions, R.K., Oxburgh, E.R., 1988. Helium, volatile fluxes and the development of continental crust. Earth Planet. Sci. Lett. 90 (3), 331–347.
Oxburgh, E.R., O'Nions, R.K., 1987. Helium loss, tectonics, and the terrestrial heat budget. Science 237 (4822), 1583–1588.
Oxburgh, E.R., O'nions, R.K., Hill, R.I., 1986. Helium isotopes in sedimentary basins. Nature 324 (6098), 632–635.
Ozima, M., Podosek, F.A., 2002. Noble Gas Geochemistry. Cambridge University Press.
Ray, M.C., Hilton, D.R., Muñoz, J., Fischer, T.P., Shaw, A.M., 2009. The effects of volatile recycling, degassing and crustal contamination on the helium and carbon geochemistry of hydrothermal fluids from the Southern Volcanic Zone of Chile. Chem. Geol. 266 (1–2), 38–49.
Rose, T.P., Davisson, M.L., 1996. Radiocarbon in hydrologic systems containing dissolved magmatic carbon dioxide. Science 273 (5280), 1367–1370.
Rose, T.P., Davisson, M.L., Criss, R.E., 1996. Isotope hydrology of voluminous cold springs in fractured rock from an active volcanic region, northeastern California. J. Hydrol. 179 (1–4), 207–236.
Saar, M.O., Castro, M.C., Hall, C.M., Manga, M., Rose, T.P., 2005. Quantifying magmatic, crustal, and atmospheric helium contributions to volcanic aquifers using all stable noble gases: Implications for magmatism and groundwater flow. Geochem. Geophys. Geosyst. 6 (3).
Sano, Y., Marty, B., 1995. Origin of carbon in fumarolic gas from island arcs. Chem. Geol. 119 (1–4), 265–274.
Sano, Y., Williams, S.N., 1996. Fluxes of mantle and subducted carbon along convergent plate boundaries. Geophys. Res. Lett. 23 (20), 2749–2752.
Seltzer, A.M., Bekaert, D.V., Barry, P.H., Durkin, K.E., Mace, E.K., Aalseth, C.E., Zappala, J.C., Mueller, P., Jurgens, B., Kulongoski, J.T., 2021. Groundwater residence time estimates obscured by anthropogenic carbonate. Sci. Adv. *7* (17) eabf3503.
Sorey, M.L., Colvard, E.M., 1994. *Measurements of heat and mass flow from thermal areas in Lassen Volcanic National Park, California, 1984-93* (p. 35). US Geological Survey, Menlo Park, CA.
Sorey, M.L., Ingebritsen, S.E., 1983. Numerical simulations of the hydrothermal system at Lassen Volcanic National Park (no. SGP-TR-74-49). US Geological Survey, Menlo Park, CA.
Sorey, M.L., Evans, W.C., Kennedy, B.M., Farrar, C.D., Hainsworth, L.J., Hausback, B., 1998. Carbon dioxide and helium emissions from a reservoir of magmatic gas beneath Mammoth Mountain, California. J. Geophys. Res. Solid Earth 103 (B7), 15303–15323.
Tardani, D., Reich, M., Roulleau, E., Takahata, N., Sano, Y., Pérez-Flores, P., Sánchez-Alfaro, P., Cembrano, J., Arancibia, G., 2016. Exploring the structural controls on helium, nitrogen and carbon isotope signatures in hydrothermal fluids along an intra-arc fault system. Geochim. Cosmochim. Acta 184, 193–211.
Varekamp, J.C., Kreulen, R., Poorter, R.P.E., Van Bergen, M.J., 1992. Carbon sources in arc volcanism, with implications for the carbon cycle. Terra Nova 4 (3), 363–373.
Visser, A., Singleton, M.J., Hillegonds, D.J., Velsko, C.A., Moran, J.E., Esser, B.K., 2012. California GAMA Special Study: A Noble Gas Membrane Inlet Mass Spectrometry (NG-MIMS) system for water and gas samples (No. LLNL-TR-548931). Lawrence Livermore National Lab.(LLNL), Livermore, CA (United States).
Visser, A., Singleton, M.J., Hillegonds, D.J., Velsko, C.A., Moran, J.E., Esser, B.K., 2013. A membrane inlet mass spectrometry system for noble gases at natural abundances in gas and water samples. Rapid Commun. Mass Spectrom. 27 (21), 2472–2482.
Vogel, J.C., Grootes, P.M., Mook, W.G., 1970. Isotopic fractionation between gaseous and dissolved carbon dioxide. Zeitschrift für Physik A Hadrons and nuclei 230 (3), 225–238.
Walter, S.R., 1986. Intermediate-focus earthquakes associated with Gorda plate subduction in northern California. Bull. Seismol. Soc. Am. 76 (2), 583–588.
Weiss, R.F., 1968, December. Piggyback sampler for dissolved gas studies on sealed water samples. In: Deep Sea Research and Oceanographic Abstracts, Vol. 15. Elsevier, pp. 695–699 no. 6.
Weiss, R.F., 1971. Solubility of helium and neon in water and seawater. J. Chem. Eng. Data 16 (2), 235–241.
Welhan, J.A., Poredai, R.J., Rison, W., Craig, H., 1988. Helium isotopes in geothermal and volcanic gases of the western United States, I. Regional variability and magmatic origin. J. Volcanol. Geotherm. Res. 34 (3–4), 185–199.
Werner, C., Kelly, P.J., Doukas, M., Lopez, T., Pfeffer, M., McGimsey, R., Neal, C., 2013. Degassing of CO2, SO2, and H2S associated with the 2009 eruption of Redoubt Volcano, Alaska. J. Volcanol. Geotherm. Res. 259, 270–284.
Werner, C., Bergfeld, D., Farrar, C.D., Doukas, M.P., Kelly, P.J., Kern, C., 2014. Decadal-scale variability of diffuse CO2 emissions and seismicity revealed from long-term monitoring (1995–2013) at Mammoth Mountain, California, USA. J. Volcanol. Geotherm. Res. 289, 51–63.
Werner, C., Fischer, T.P., Aiuppa, A., Edmonds, M., Cardellini, C., Carn, S., Chiodini, G., Cottrell, E., Burton, M., Shinohara, H., Allard, P., 2019. Carbon Dioxide Emissions from Subaerial Volcanic Regions. In Deep carbon past to present. Cambridge University Press.
Wilde, F.D., Radtke, D.B. (Eds.), 1998. Handbooks for Water-Resources Investigations: National Field Manual for the Collection of Water-Quality Data. *Field measurements*. US Department of the Interior, US Geological Survey.
Williams, S.N., Schaefer, S.J., Calvache, V.M.L., Lopez, D., 1992. Global carbon dioxide emission to the atmosphere by volcanoes. Geochim. Cosmochim. Acta 56 (4), 1765–1770.
Wills, C.J., 1991. Active faults north of Lassen Volcanic National Park, northern California. Calif. Geol. 44 (3), 51–58.